npj | climate and atmospheric science

Article

Published in partnership with CECCR at King Abdulaziz University

https://doi.org/10.1038/s41612-026-01439-z

Towards a theoretical understanding of Arctic amplification dynamics

Masoud Rostami[1,2,3] ✉, Bijan Fallah[3], Farahnaz Fazel-Rastgar[4], Mehdi Hamidi[5,6], Saeed Hariri[7], Junxin Guo[8] & Li-Yun Fu[1,9] ✉

This paper develops a theoretical framework for understanding Arctic amplification through the lens of nonlinear potential vorticity (PV) dynamics, static stability feedbacks, and stratosphere-troposphere coupling. Using scaling arguments, Green's function solutions, and a modified Eady model, we show how surface-warming-induced static stability perturbations modulate PV inversion efficiency and extend remote influences. We identify a critical threshold in the diabatic number $\mathcal{D}$ that marks the transition from a dry-nonlinear to a moist-nonlinear regime where diabatic PV generation outweighs baroclinic advection. A regime diagram constructed from the nonlinearity ratio $\mathcal{R} = |\sigma'/\overline{\sigma}|$ (where σ is static stability) and $\mathcal{D}$ reveals four quadrants; the Arctic already resides in a nonlinear background ($\mathcal{R}$>0.3 for most CMIP6 models) and under continued warming, it migrates vertically into the moist-nonlinear state via increasing $\mathcal{D}$. Under SSP2-4.5, the ensemble-mean $\mathcal{D}$ crosses the 0.03 threshold by mid-century ($\mathcal{D} = 0.031$); under SSP5-8.5, $\mathcal{D}$ reaches 0.039 by end-century, with 88% of models exceeding the threshold. Reduced stability amplifies baroclinic growth rates and shifts most unstable modes toward high-latitude blocking wavelengths. Extending the framework to the stratosphere, we show that the refractive index for vertically propagating Rossby waves decreases with weakened zonal winds, a robust signal across models, enabling deeper wave penetration. Observational support from ERA5 reanalysis reveals a vertical contrast in PV anomalies - strong positive anomalies in the lower troposphere and a wave-like pattern aloft, consistent with the transition to diabatically driven dynamics. A positive feedback loop linking surface warming, reduced stability, enhanced inversion efficiency, amplified streamfunction anomalies, increased poleward heat transport, and strengthened vertical wave coupling suggests a loop gain that would be arrested by nonlinear saturation. These results establish polar amplification as arising from coupled interactions of static stability, PV dynamics, diabatic heating, and stratosphere-troposphere coupling, with direct implications for predicting midlatitude extreme weather events.

Polar amplification, the phenomenon where high latitudes warm disproportionately compared to the global mean, represents one of the most robust and consequential signatures of anthropogenic climate change[1–4]. Observational evidence indicates that the Arctic has warmed nearly four times faster than the global average over recent decades[5], with profound implications for sea ice retreat, permafrost degradation, and ecosystem transformation[6]. Figure 1 synthesises observational and model-based evidence for Arctic amplification. Panels (a–c) show the spatial pattern of near-surface warming from ERA5 reanalysis, NOAA GlobalTemp, and the CMIP6 multi-model mean, respectively. Panel (d) displays the

[1]School of Geosciences, China University of Petroleum (East China), Qingdao, P. R. China. [2]Laboratoire de Météorologie Dynamique (LMD)/IPSL, ENS-PSL Université, Ecole Polytechnique-Institut Polytechnique de Paris, Sorbonne Université, CNRS, Paris, France. [3]Potsdam Institute for Climate Impact Research (PIK), Member of the Leibniz Association, Potsdam, Germany. [4]School of Chemistry and Physics, University of KwaZulu Natal, Durban, South Africa. [5]Institute for Geophysics and Meteorology, University of Cologne, Cologne, Germany. [6]Faculty of Civil Engineering, Babol Noshirvani University of Technology, Babol, Iran. [7]Leibniz Institute for Baltic Sea Research Warnemünde, Rostock, Germany. [8]MSU-BIT-SMBU Joint Research Center of Applied Mathematics, Shenzhen MSU-BIT University, Shenzhen, China. [9]Qingdao National Laboratory for Marine Science and Technology, Qingdao, P. R. China. ✉e-mail: mrostami@lmd.ens.fr; lfu@upc.edu.cn

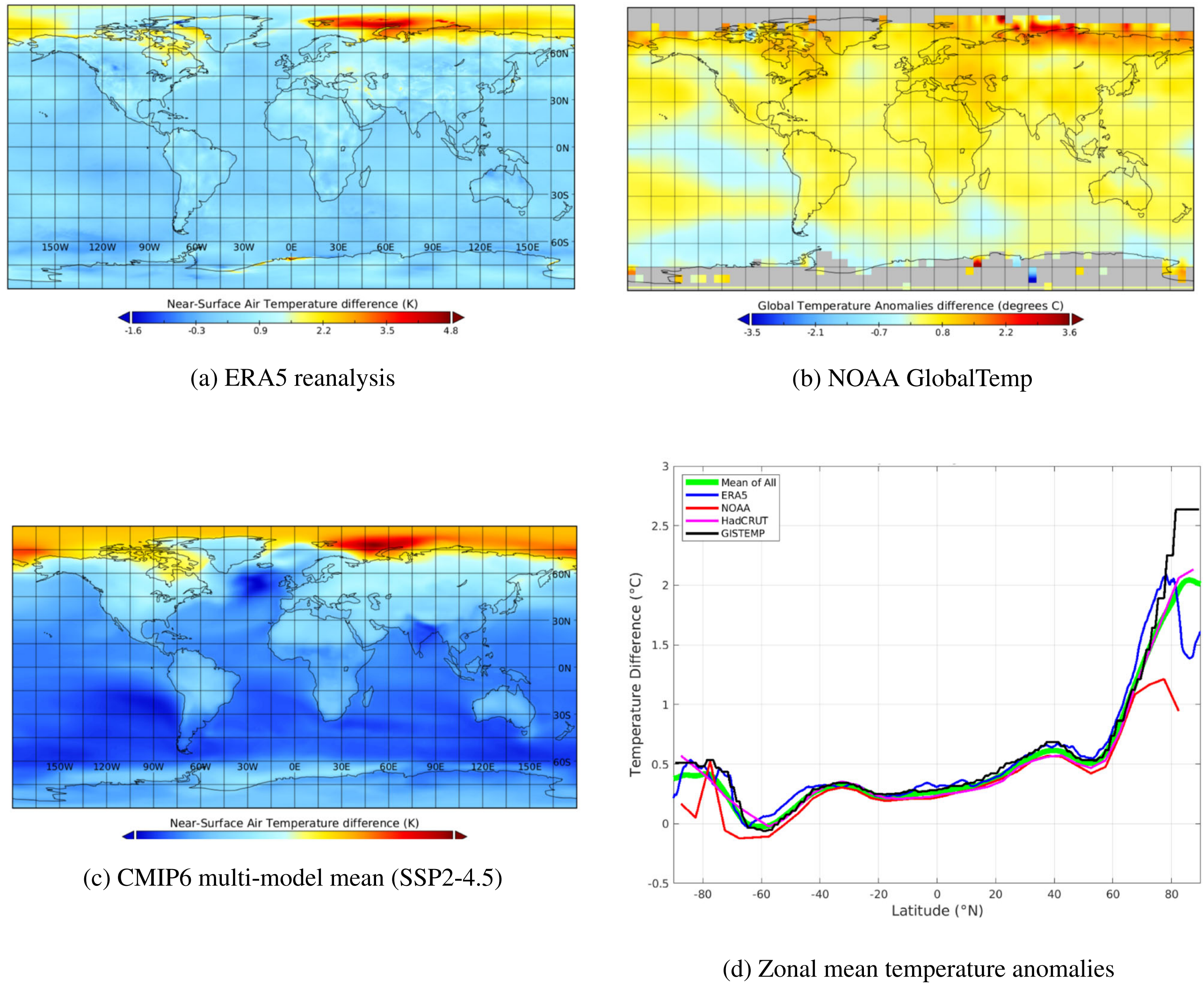

Fig. 1 | Observed and simulated Arctic amplification. **a–c** Spatial distribution of near-surface temperature anomalies (°C) for the period 2006–2024 relative to 1986–2005 from **a** ERA5 reanalysis, **b** NOAA GlobalTemp, and **c** CMIP6 multi-model mean under SSP2-4.5. **d** Zonal mean temperature anomalies from ERA5 (blue), NOAA (orange), HadCRUT, and GISTEMP (ensemble mean thick green). All datasets consistently show 2–3× stronger warming north of 60° N compared to the tropics, with inter-product differences below 0.5° C.

corresponding zonal-mean temperature anomalies, confirming that warming north of 60° N is approximately 2–3 times stronger than in the tropics, with remarkable consistency across datasets (inter-product differences < 0. 5° C). An estimate of the observational uncertainty associated with the ERA5 data is provided in the Supplementary Information (SI, Fig. 1). Together, these panels establish the robust, large-scale signature of polar amplification that motivates the theoretical developments of this study.

While the existence of polar amplification is well-documented across observations and climate models[7,8], the underlying dynamical and thermodynamic mechanisms remain incompletely understood, leaving a critical gap in our ability to predict future Arctic and midlatitude climate extremes with confidence[9]. Traditional explanations have emphasised thermodynamic processes, particularly radiative feedbacks such as the surface albedo feedback from diminishing ice and snow cover[10,11], and the temperature-dependent increase in atmospheric water vapour[12]. The lapse rate feedback, wherein the vertical structure of warming modulates outgoing longwave radiation, has also been identified as a key contributor[2,13]. However, these thermodynamic processes alone cannot fully account for the spatial and temporal patterns of polar warming evident in Fig. 1, nor its coupling to midlatitude circulation changes[14,15]. A growing body of evidence points to the need for a deeper theoretical foundation that integrates radiative feedbacks with the dynamics of atmospheric circulation, including the role of baroclinic eddies, potential vorticity (PV) dynamics, and diabatic processes such as latent heat release[16,17].

Recent large-scale observational programs, such as the (AC)^3 project, have documented distinct atmospheric moistening, increased regional storm activity, and amplified winter warming in the Svalbard and North Pole regions[6]. These findings underscore the need for theoretical frameworks capable of explaining not only the magnitude of Arctic warming but also its vertical structure, seasonal evolution, and connection to extreme weather events at midlatitudes[18]. The substantial inter-model spread in Arctic climate projections further emphasises that a quantitative process understanding remains elusive[19–22].

This paper develops a theoretical framework that reinterprets polar amplification through the integrated lens of nonlinear PV dynamics, static stability feedbacks, diabatic PV generation, Rossby wave resonance, and stratosphere-troposphere coupling. In doing so, we address several fundamental gaps in current understanding. First, while previous studies have recognised the importance of static stability changes[2], the nonlinear feedback whereby stability perturbations modulate PV inversion efficiency has remained largely unexplored. Second, the transition from a dry, baroclinically-driven regime to a moist, diabatically-dominated one has been observed[6] but lacks a theoretical grounding that identifies critical thresholds and bifurcation structures. Third, the mechanistic links between

Fig. 2 | Dynamical regime diagram for the Arctic atmosphere in the space of the nonlinearity ratio $\mathcal{R} = |\sigma'/\overline{\sigma}|$ and the diabatic number $\mathcal{D}$. Four quadrants define dry/moist and linear/nonlinear regimes (thresholds $\mathcal{R} = 0.3$, $\mathcal{D} = 0.03$). Small translucent markers show individual CMIP6 models; large symbols with error bars show scenario-period ensemble means. Reanalysis baselines (ERA5, NCEP/NCAR-R1) are shown in black/grey for three climatological periods. The trajectory from historical (blue) through SSP2-4.5 (orange) to SSP5-8.5 (red) illustrates the systematic vertical migration into the moist-nonlinear regime under continued warming, driven primarily by increasing $\mathcal{D}$.

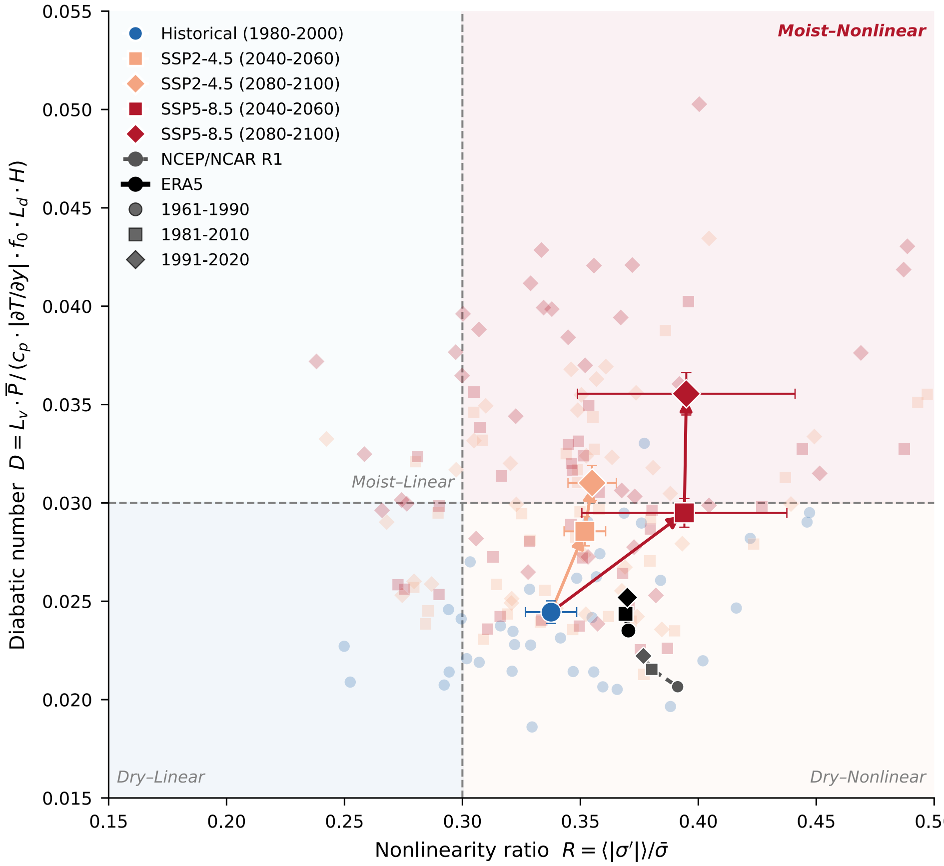

Arctic amplification and the increased persistence of high-latitude blocking patterns have not been systematically derived from first principles.

Our analysis suggests that Arctic warming involves more than just a passive thermodynamic response to radiative forcing; it can be understood as an active dynamical process driven by self-reinforcing feedbacks involving static stability, wave-mean flow interactions, and diabatic heating. The framework is built upon three interconnected pillars: (i) nonlinear PV-stability interactions, captured through the nonlinearity ratio $\mathcal{R} = |\sigma'/\overline{\sigma}|$, which quantifies the background nonlinearity of the system; (ii) diabatic PV generation through latent heating, quantified through a moist Eady growth framework that explains how the Arctic transforms from a dry, baroclinically-driven regime to a moist, diabatically-dominated one despite weakened meridional temperature gradients; and (iii) the reorganization of eddy-mean flow interactions, including the emergence of multiple dynamical regimes characterized by a regime diagram with four quadrants. Within this framework, we show that the critical transition is governed by the diabatic number $\mathcal{D}$, which increases robustly under warming, pushing the system from a dry-nonlinear into a moist-nonlinear state.

A key innovation of our study is the introduction of a framework to derive quantitative thresholds that delineate regime transitions. Using scaling arguments from baroclinic instability theory, Green's function solutions of the PV inversion operator, and linear stability analysis of a modified Eady model, we quantify how reduced static stability under warming extends the range of PV influence, amplifies wave growth, and shifts the most unstable modes toward wavelengths characteristic of high-latitude blocking (≈4000 km). We identify a critical nonlinearity ratio $\mathcal{R} \approx 0.3$, marking the onset of subcritical instability, where the Landau coefficient becomes negative; this threshold is already exceeded in the majority of CMIP6 historical simulations, implying that the Arctic atmosphere is preconditioned for nonlinear amplification. The warming-induced increase in $\mathcal{D}$ then provides the diabatic energy that enables this nonlinear potential to be realised.

Our theoretical framework further extends to stratosphere-troposphere coupling[23–25]. We show that the refractive index for vertically propagating Rossby waves decreases with weakening zonal winds, a robust response to reduced meridional temperature gradients, providing a dynamical explanation for the observed increase in sudden stratospheric warming (SSW) frequency[26,27] and its connection to sea ice loss. The combination of strong background nonlinearity ($\mathcal{R} > 0.3$) and vigorous diabatic forcing ($\mathcal{D} > 0.03$) enables a deep stratospheric response, linking Arctic amplification to stratospheric variability.

The bifurcation framework captures the transition between dry linear, dry nonlinear, moist linear, and moist nonlinear regimes. The current Arctic resides in the dry-nonlinear regime (most models have $\mathcal{R} > 0.3$, $\mathcal{D} < 0.03$) and under continued warming, it moves into the moist-nonlinear regime where diabatic forcing dominates. This trajectory explains observed intensifications in diabatic storm processes[6] and provides a basis for understanding why climate models exhibit such a large spread in their projections–they differ in how they represent the feedback strengths that govern these regime transitions[22].

Our results highlight the importance of representing nonlinear dynamical feedbacks in climate projections, particularly as moisture-dependent processes become increasingly dominant under continued warming. By providing testable parameterisations for eddy diffusivity, PV inversion efficiency, and polar amplification indices, this work aims to reduce the substantial uncertainty in Arctic climate projections[9] and improve assessments of regional climate impacts associated with continued Arctic warming.

Results

A dynamical phase space for regime transition in Arctic amplification

The regime diagram (Fig. 2) organises the Arctic atmosphere into four quadrants defined by two physically grounded dimensionless parameters:

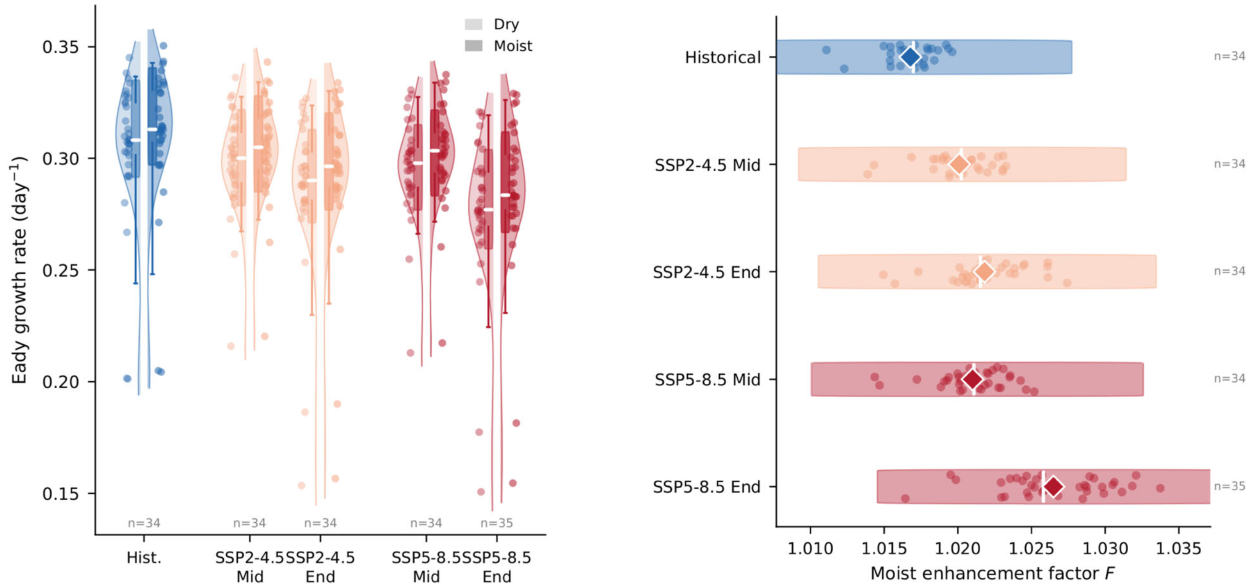

(a) Baroclinic instability

(b) Moist enhancement by scenario

Fig. 3 | Baroclinic instability response across CMIP6 models. a Split-violin raincloud plots of absolute Eady growth rate (day^{-1}) for dry (left half, lighter shading) and moist (right half, darker shading) formulations. Groups: historical (1980–2000, blue), SSP2-4.5 mid- and end-century (orange), SSP5-8.5 mid- and end-century (red). Each group shows the kernel density estimate (half-violin), interquartile range with 5th--95th percentile whiskers (box), and individual model values (jittered dots). n denotes the number of CMIP6 models per group. **b** Moist enhancement factor $F = \sigma_{E,\mathrm{moist}}/\sigma_{E,\mathrm{dry}}$ by scenario and period. Each row shows individual model dots, IQR box (shaded), median (white line), and multi-model mean (diamond). The systematic rightward shift from Historical ($F \approx 1.017$) to SSP5-8.5 end-century ($F \approx 1.027$) reflects Clausius-Clapeyron scaling of latent heat release under warming. Models filtered by $\mathcal{R} < 1.5$ and $\sigma_{E,\mathrm{dry}} > 0.01$ day^{-1}; MCM-UA-1-0 excluded.

the nonlinearity ratio $\mathcal{R} = |\sigma'/\overline{\sigma}|$ and the diabatic number $\mathcal{D}$. The nonlinearity ratio quantifies the strength of static stability perturbations relative to the climatological background; values $\mathcal{R} > 0.3$ indicate that nonlinear PV-stability feedbacks are comparable to or exceed linear processes, enabling subcritical instability (see the 'Nonlinear amplitude dynamics and subcritical instability' section). The diabatic number $\mathcal{D}$ measures the competition between diabatic PV generation and baroclinic advection, derived from the eddy PV variance budget (Eq. 32). Values $\mathcal{D} \ll 1$ indicate dry baroclinic dominance; as $\mathcal{D}$ approaches and exceeds ≈ 0.03, latent heating begins to control the PV dynamics, with positive feedbacks amplifying its dynamical consequences over synoptic timescales.

The diagram is divided by critical thresholds $\mathcal{R} = 0.3$ and $\mathcal{D} = 0.03$, derived from scaling analysis of the Landau coefficient (see the 'Nonlinear PV dynamics and Landau equation' subsection in Methods). The four quadrants thus correspond to distinct dynamical regimes: dry linear ($\mathcal{R} < 0.3$, $\mathcal{D} < 0.03$), where classical dry baroclinic instability operates; dry nonlinear ($\mathcal{R} > 0.3$, $\mathcal{D} < 0.03$), where nonlinear PV dynamics are important but diabatic effects remain weak; moist linear ($\mathcal{R} < 0.3$, $\mathcal{D} > 0.03$), where diabatic processes contribute without triggering subcritical instability; and moist nonlinear ($\mathcal{R} > 0.3$, $\mathcal{D} > 0.03$), where both nonlinear PV feedbacks and vigorous diabatic forcing coexist, enabling subcritical instability and explosive wave growth.

The historical Arctic (blue symbols in Fig. 2) resides predominantly in the dry-nonlinear quadrant. The multi-model mean historical $\mathcal{R}$ is 0.41 (median 0.38), with 67% of individual models exceeding the $\mathcal{R} = 0.3$ threshold. Historical $\mathcal{D}$ averages 0.02 (median 0.021), placing the system slightly below the diabatic threshold. Under contemporary warming (SSP2-4.5, orange), the ensemble mean shifts primarily upward: $\mathcal{D}$ crosses the 0.03 threshold, indicating that diabatic processes have become dynamically significant, while $\mathcal{R}$ remaining essentially unchanged (median change $\Delta\mathcal{R} = -0.014$, $p = 0.27$). Under high-emission scenarios (SSP5-8.5, red), the trajectory moves decisively into the moist-nonlinear regime, with $\mathcal{D} > 0.03$ for all models and $\mathcal{R}$ still near historical values. Individual CMIP6 models (small translucent markers) and reanalysis baselines (ERA5 and NCEP/NCAR R1, black/grey) confirm this systematic vertical migration across the ensemble, demonstrating the robustness of the increase in $\mathcal{D}$ despite structural uncertainties. The inter-model spread in historical $\mathcal{R}$ (range 0.24-0.86) and $\mathcal{D}$ (range 0.015-0.028) is partly explained by model resolution and model-top height. High-resolution models tend to produce larger $\mathcal{R}$, while high-top models show somewhat different $\mathcal{D}$ distributions (SI, Fig. 5). Nevertheless, the regime transition, a robust increase in $\mathcal{D}$ with warming, is consistent across all categories. This indicates that the critical threshold $\mathcal{D}_c \approx 0.03$ is not sensitive to model resolution or top height, supporting its physical relevance.

Thus, the key regime transition under warming is not a crossing of the $\mathcal{R} = 0.3$ line, which was already crossed in the pre-industrial climate, but rather a shift from a dry-nonlinear to a moist-nonlinear state driven by increasing $\mathcal{D}$. This reinterpretation has profound implications. First, the fact that $\mathcal{R} > 0.3$ is widespread historically implies that the Arctic atmosphere is inherently preconditioned for nonlinear wave amplification; subcritical instability is possible even without additional forcing. Second, the robust increase in $\mathcal{D}$ with warming means that diabatic PV generation now dominates over baroclinic production, fundamentally altering storm dynamics: cyclones intensify through latent heat release rather than baroclinic conversion, leading to more rapid deepening, higher peak intensities, and increased precipitation efficiency[6]. Third, the combination of strong background nonlinearity ($\mathcal{R} > 0.3$) and vigorous diabatic forcing ($\mathcal{D} > 0.03$) enhances two-way connectivity between the Arctic and midlatitudes: PV anomalies generated by diabatic processes in the Arctic propagate equatorward and modulate jet stream variability, while midlatitude wave activity penetrates more deeply into the Arctic stratosphere (see the 'Rossby wave propagation and stratospheric coupling' section). The regime diagram thus provides a unified dynamical framework for interpreting the observed intensification of extreme weather under Arctic amplification, explaining why the system has crossed a qualitative threshold in

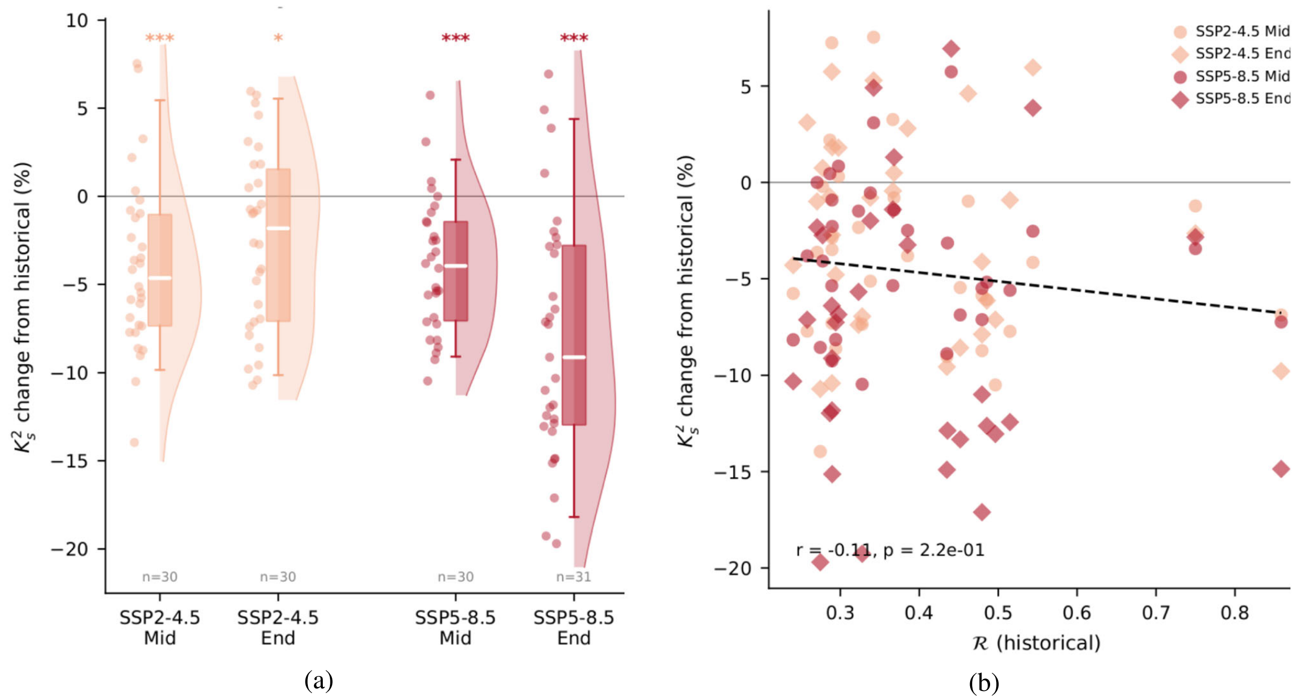

Fig. 4 | Rossby wave propagation diagnostics across CMIP6 models. a Percentage change in the stationary wave refractive index K_s^2 at 250 hPa relative to the historical period (1980–2000). Raincloud plots show kernel density (half-violin), IQR with 5th--95th percentile whiskers, and individual model values. Significance asterisks from Wilcoxon signed-rank tests (H_0: median change = 0): $p < 0.001$, $p < 0.01$, $p < 0.05$. **b** Scatter of historical nonlinearity ratio $\mathcal{R}$ vs percentage change in K_s^2. Each point represents one CMIP6 model under a given scenario and time period; circles denote mid-century, diamonds end-century; colours distinguish SSP2-4.5 (orange) and SSP5-8.5 (red). Dashed line: pooled ordinary least-squares regression ($r = -0.11$, $p = 0.22$). The weak correlation indicates that the refractive index reduction is not driven by changes in $\mathcal{R}$; rather, it reflects the robust weakening of zonal winds due to reduced meridional temperature gradients. MCM-UA-1-0 and MPI-ESM1-2-HR were excluded from both panels.

diabatic forcing with consequences for storm behaviour, blocking persistence, and stratosphere-troposphere coupling.

Baroclinic instability response across CMIP6 models

The contrasting behaviour of dry and moist growth rates has profound implications for Arctic amplification. Although the dry baroclinic energy source weakens, the enhanced latent heat release acts as a potent alternative energy source, enabling storms to intensify through diabatic processes rather than baroclinic conversion. This shift toward a moist diabatic regime explains the observed tendency toward "fewer but stronger" cyclones in a warming Arctic[6] and aligns with the regime transition identified in Fig. 2.

The multi-model dry Eady growth rate $\sigma_E = 0.31\ (f/N)\ |\partial u/\partial z|$ (Fig. 3a) decreases systematically from a historical ensemble mean of ~0.305 day^{-1} to ~0.277 day^{-1} under SSP5-8.5 end-century conditions, a reduction of approximately 9%. This decline is consistent with the theoretical expectation that polar amplification weakens the meridional temperature gradient and hence the vertical wind shear that drives baroclinic instability. The moist Eady growth rate, computed using moist static stability according to the modified Eady model (see the 'Eady growth rate diagnostics' subsection in 'Methods'), shows a parallel decline but is systematically offset to higher values, reflecting the compensating role of latent heat release. The split-violin distributions reveal tight peaks near the multi-model median with extended tails toward larger reductions, indicating that while the sign of the response is robust, its magnitude varies substantially across models.

The moist enhancement factor $\mathcal{F} = \sigma_{E,\text{moist}}/\sigma_{E,\text{dry}}$ (Fig. 3b) exhibits a systematic rightward shift from $\mathcal{F} \approx 1.017$ in the historical period to $\mathcal{F} \approx 1.027$ under SSP5-8.5 end-century forcing. This ~ 0.5% increase in $\mathcal{F}$ per degree of Arctic warming is consistent with Clausius-Clapeyron scaling of latent heat release, confirming the theoretical prediction that diabatic processes increasingly compensate for reduced dry baroclinicity. The inter-model spread narrows under stronger forcing, suggesting convergence in the moisture response even as models disagree on the magnitude of dry instability changes. While the absolute increase in $\mathcal{F}$ is modest (~1%), it is statistically robust across the ensemble and aligns with the expected thermodynamic response under warming. However, it is the increase in the diabatic number $\mathcal{D}$, which exhibits 100% model agreement and a clear threshold crossing (Fig. 2), that marks the qualitative shift to a moist-dominated regime. The change in $\mathcal{F}$ serves as supporting evidence that moist processes are becoming more important, but the primary indicator of regime transition remains the robust increase in $\mathcal{D}$.

Rossby wave propagation and stratospheric coupling

The coupling between the troposphere and stratosphere represents a critical pathway through which Arctic amplification can influence the large-scale circulation and, in turn, feed back onto surface climate[23–25]. Rossby waves generated in the troposphere can propagate vertically into the stratosphere when the background flow satisfies the Charney–Drazin criterion[28,29]: vertical propagation occurs for stationary waves when the zonal wind is westerly and weaker than a critical value, and the refractive index squared $n^2 > 0$. The refractive index governs the vertical and meridional propagation characteristics of planetary waves; a decrease in the stationary wavenumber squared K_s^2 (which is proportional to n^2) implies enhanced poleward wave focusing and increased vertical penetration, favouring wave breaking in the stratosphere and the deceleration of the polar night jet, a precursor to SSW events.

The stationary wave refractive index K_s^2 at 250 hPa (Fig. 4a) exhibits a robust negative trend across the CMIP6 ensemble: the median percentage change ranges from −4% (SSP2-4.5 mid-century) to −8% (SSP5-8.5 end-century), with statistically significant reductions in all four scenario-period combinations (Wilcoxon signed-rank test, $p < 0.05$). The strongest signal emerges under SSP5-8.5 end-century conditions ($p < 0.001$), confirming that refractive index changes scale with warming magnitude.

The reduction in K_s^2 is primarily attributable to the weakening of the upper-level zonal wind $\overline{u}$–a thermal wind response to the reduced

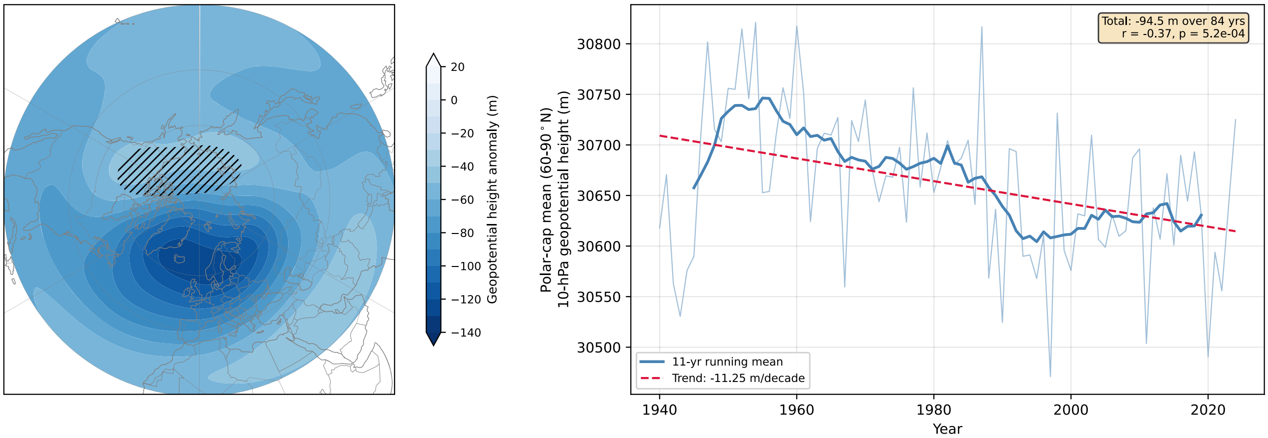

(a) Geopotential height anomaly (m)

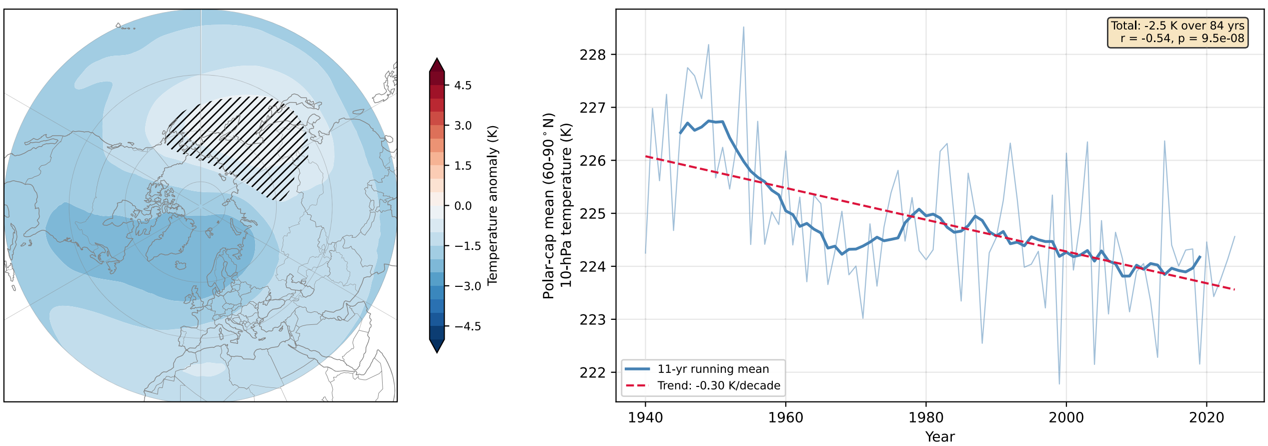

(b) Temperature anomaly (K)

Fig. 5 | Variation of the Arctic stratospheric polar vortex. a ERA5 10-hPa geopotential height anomaly (m) between recent (1995–2024) and historical (1941–1970) periods. Hatching indicates areas where the change is not statistically significant ($p \geq 0.05$, Welch t-test on annual means). Inset: polar-cap mean (60–90° N) annual time series showing a significant height decrease of −11.3 m/decade ($r = -0.37$, $p = 5.2 \times 10^{-4}$). **b** Same as (**a**) but for temperature (K). The polar-cap mean cooling trend is −0.30 K/decade ($r = -0.54$, $p = 9.5 \times 10^{-8}$); 90% of Northern Hemisphere grid points show a statistically significant cooling. The combined height decrease and cooling are the dynamical fingerprint of a strengthened stratospheric polar vortex.

meridional temperature gradient—rather than to changes in the non-linearity ratio $\mathcal{R}$. Indeed, the cross-model correlation between historical $\mathcal{R}$ and the projected percentage change in K_s^2 is weak and non-significant ($r = -0.11$, $p = 0.22$; Fig. 4b). Within-model changes show a positive correlation (Spearman $\rho = +0.47$, $p = 0.007$), opposite to the sign expected if increasing $\mathcal{R}$ drove stronger K_s^2 reductions. Thus, while the refractive index decrease is robust and consistent with deeper wave penetration, it is not causally linked to $\mathcal{R}$ in the multi-model ensemble. Instead, it follows directly from the thermal wind adjustment, a mechanism well established in previous literature.

Projected changes in mean sea level pressure provide further evidence for these dynamical feedbacks under long-term future warming scenarios (SI, Fig. 3). Across all four SSPs, negative pressure anomalies dominate the Arctic basin, indicating a strengthening of the cyclonic circulation and a deepening of the polar vortex (i.e. lower geopotential heights in the stratosphere). The magnitude and spatial extent of these anomalies scale systematically with the strength of radiative forcing: under the highest-emission SSP5-8.5, pressure drops exceed −2.5 hPa over large areas of the central Arctic and Barents–Kara Seas, while the low-emission SSP1-1.9 shows more moderate changes within the −1.0 to −1.5 hPa range. Notably, positive pressure anomalies emerge over the North Atlantic sector in the higher emission scenarios (SSP3-7.0 and SSP5-8.5), suggesting a dipole response that may modulate the North Atlantic Oscillation and associated storm tracks. This pattern aligns with our theoretical prediction that reduced static stability and enhanced upward wave propagation (Eq. 10) lead to a deceleration of the polar night jet and a more cyclonic surface circulation, with the strongest anomalies coinciding with regions of maximum sea-ice loss and ocean-atmosphere heat exchange. The expansion of the negative anomaly footprint from the near-term to the long-term period demonstrates the cumulative nature of the dynamical feedbacks. These projected pressure trends have important implications for mid-latitude weather: a strengthened polar vortex tends to confine cold air to high latitudes, reducing the likelihood of extreme cold outbreaks in Eurasia and North America, whereas a weakened vortex (positive anomalies) would favour blocking episodes[14,30].

This stratospheric strengthening is independently confirmed by ERA5 10 hPa geopotential height and temperature anomalies (Fig. 5). The figure shows that 88% of Northern Hemisphere grid points exhibit a statistically significant height reduction at 10 hPa, with a polar-cap mean weakening trend of −11.3 m/decade ($r = -0.37$, $p = 5.2 \times 10^{-4}$). The accompanying

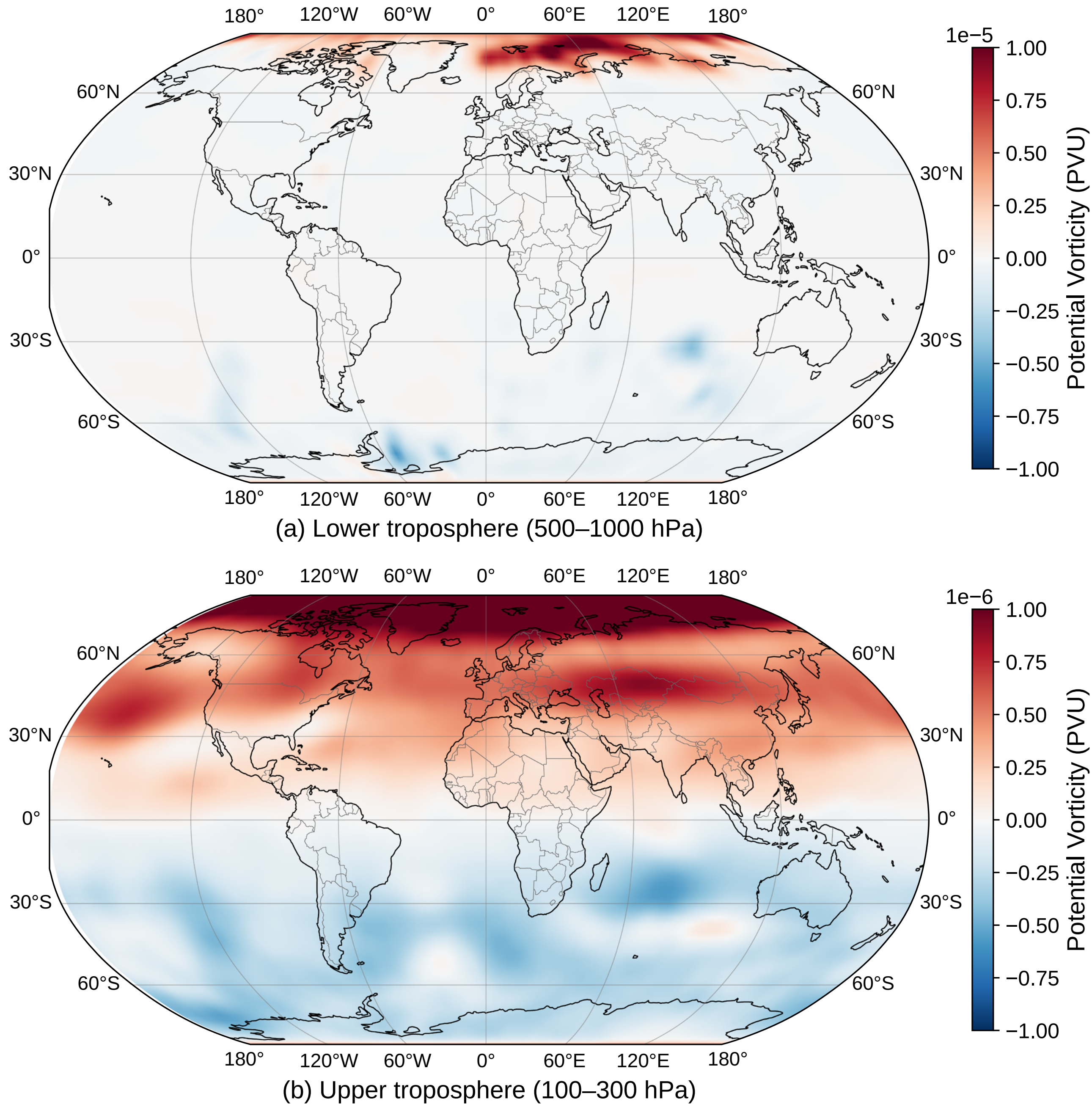

Fig. 6 | PV anomalies (PVU) between recent (1995–2024) and historical (1941–1970) periods from ERA5 reanalysis. a Lower-tropospheric anomalies (500–1000 hPa). Positive anomalies (red) dominate Arctic regions, with values ranging from −3 to +2 PVU. Higher values over oceans reflect enhanced diabatic PV generation from latent heat release. **b** Upper-tropospheric anomalies (100–300 hPa). Alternating positive and negative bands in the midlatitudes (colour scale −1.0 to +1.0 PVU, multiplied by 10^{-6}) indicate shifts in the jet stream and Rossby wave train patterns associated with altered waveguidance. The vertical contrast in layer-mean PV—strong low-level positive anomalies coupled with upper-level wave trains.

stratospheric cooling at 10 hPa shows a polar-cap trend of −0.30 K/decade ($r = -0.54$, $p = 9.5 \times 10^{-8}$), with 90% of Northern Hemisphere grid points significant. The combined height decrease and cooling are the dynamical fingerprint of a strengthened stratospheric polar vortex.

Vertical structure of PV anomalies

The vertical structure of PV anomalies provides critical observational evidence for the regime shift from dry baroclinic to moist diabatic dynamics under Arctic amplification. According to the theoretical framework developed in the 'A dynamical phase space for regime transition in Arctic amplification' and 'Baroclinic instability response across CMIP6 models' sections, enhanced latent heat release in a warming Arctic should manifest as positive PV anomalies in the lower troposphere, where condensation occurs, while the upper-level circulation adjusts to maintain thermal wind balance, producing characteristic wave train patterns in the midlatitudes. This vertical contrast in layer-mean PV (i.e. strong positive PV in the lower troposphere and a wave-modulated pattern aloft) is a direct consequence of diabatic PV generation: from Ertel's theorem, latent heating generates PV through the term $(\nabla\theta \times \nabla\dot{\theta}) \cdot \mathbf{k}$, which is maximised in regions of strong vertical gradients of heating, precisely where condensation occurs in ascending air streams. The mcTRSW model (see the 'Condensation-driven PV dynamics: insights from the mcTRSW model' subsection in 'Methods') provides a conceptual illustration of this mechanism, showing that condensation acts as a positive PV source in the lower layer and a sink aloft,

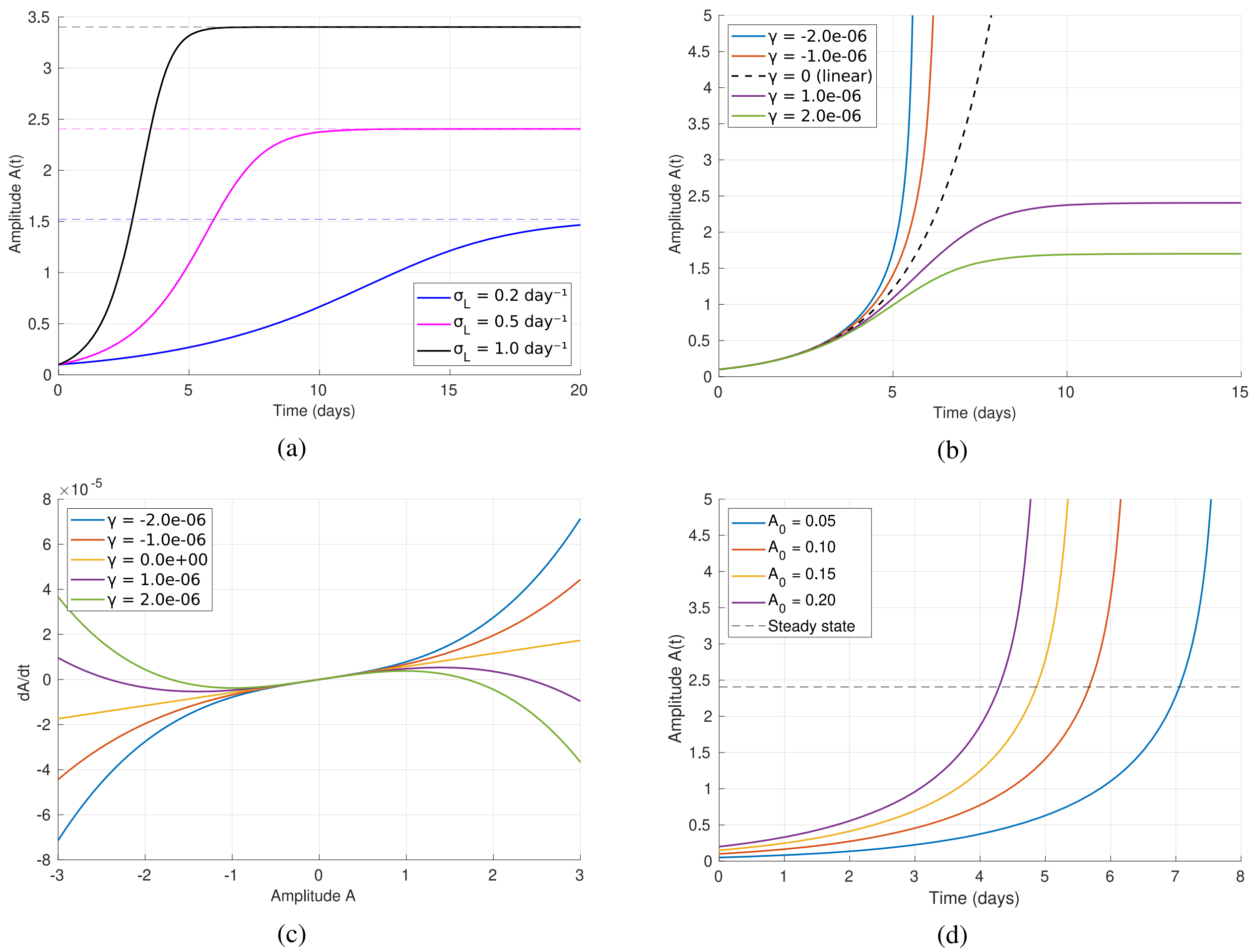

Fig. 7 | Nonlinear amplitude dynamics described by the Landau equation $\frac{dA}{dt} = \sigma_L A - \gamma |A|^2 A$. **a** Sensitivity to the linear growth rate σ_L (fixed $\gamma = 1 \times 10^{-6}$ s^{-1}, $A_0 = 0.1$). Larger σ_L yields faster growth and higher saturated amplitude $A_\infty = \sqrt{\sigma_L/\gamma}$ (dashed lines). **b** Time evolution for different values of the nonlinear coefficient γ (fixed $\sigma_L = 0.5$ day^{-1}, $A_0 = 0.1$). Positive γ leads to saturation; $\gamma = 0$ gives unbounded exponential growth; negative γ produces finite-time blowup, the hallmark of subcritical instability. **c** Phase portrait ($\frac{dA}{dt}$ vs A) for the same γ values. For $\gamma > 0$, the nonzero fixed points $\pm\sqrt{\sigma_L/\gamma}$ are stable (supercritical bifurcation); for $\gamma < 0$, they disappear, and trajectories with sufficiently large initial amplitude grow without bound. **d** Subcritical regime ($\gamma = -1 \times 10^{-6}$ s^{-1}): amplitude evolution for various initial values A_0. Only amplitudes above a critical threshold trigger explosive growth; smaller disturbances decay. This threshold behaviour mirrors the condition $\mathcal{R} > 0.3$ derived from our scaling analysis, providing a dynamical explanation for the transition from damped to amplified wave regimes under Arctic amplification and for the explosive growth of planetary waves prior to SSW events.

creating a robust vertical contrast that persists even under varying background conditions.

Figure 6 compares lower- and upper-tropospheric PV anomalies between recent (1995–2024) and historical (1941–1970) periods from ERA5 reanalysis. The lower-tropospheric anomalies (500–1000 hPa, panel a) exhibit strong positive values dominating the Arctic region, with magnitudes reaching +2 PVU over the Barents–Kara Seas, the Labrador Sea, and the Bering Strait. These positive anomalies are particularly pronounced over oceanic areas, consistent with enhanced latent heat release from increased moisture availability and cyclonic activity. The spatial pattern aligns remarkably well with regions of maximum sea-ice loss and ocean-atmosphere heat exchange documented in recent observational studies[6], providing direct evidence for the coupling between surface warming, moisture increase, and diabatic PV generation.

In striking contrast, the upper-tropospheric anomalies (100–300 hPa, panel b) exhibit a complex, wave-like pattern with alternating positive and negative bands across the midlatitudes. This structure, with anomalies scaled by 10^{-6} PVU, reflects shifts in the jet stream and changes in Rossby wave guidance associated with altered refractive indices (see the 'Rossby wave propagation and stratospheric coupling' section). The wave train pattern, extending from the North Pacific across North America to the North Atlantic, indicates that Arctic-amplified diabatic forcing is not confined to high latitudes but projects onto planetary-scale teleconnection patterns. This provides observational confirmation of the enhanced two-way connectivity between the Arctic and midlatitudes predicted by our regime diagram for the moist nonlinear regime (the 'A dynamical phase space for regime transition in Arctic amplification' section). The wave-like pattern is further supported by the zonal-mean PV profile (SI Fig. 2), which shows a clear vertical contrast consistent with a forced Rossby wave train. The vertical contrast in layer-mean PV shows strong low-level positive anomalies coupled with upper-level wave trains. Under dry baroclinic instability, PV anomalies are typically equivalent barotropic or have opposite signs in the upper and lower troposphere associated with baroclinic growth. Here, the observed pattern is fundamentally different: low-level PV is generated diabatically and locally, while the upper-level response is dominated by Rossby wave propagation and adjustment. This vertical contrast serves as a fingerprint of the regime shift identified in our theoretical framework, suggesting that the Arctic has entered a state where diabatic processes play a dominant role in shaping the large-scale circulation. The qualitative consistency between the observed PV anomalies and the conceptual illustration provided by the mcTRSW model (the 'Condensation-driven PV dynamics: insights from the mcTRSW model' subsection) further supports the mechanistic link between condensation, PV generation, and the vertical contrast in PV. The zonal-mean PV profile (SI Fig. 2) illustrates this vertical contrast more directly.

The projected changes in Arctic precipitation (SI, Fig. 4) provide additional evidence for the moistening of the Arctic atmosphere and its coupling to the dynamical feedbacks described above. Across all five SSP scenarios, widespread increases in daily accumulated precipitation dominate the Arctic basin, with the magnitude and spatial extent scaling systematically with emission strength. Under the highest-emission SSP5-8.5, precipitation anomalies exceed 0.8 mm day^{-1} over the Barents–Kara Seas, the central Arctic Ocean, and coastal Greenland, regions coinciding with maximum sea-ice loss and enhanced ocean-atmosphere heat exchange. The mcTRSW model further elucidates this mechanism, demonstrating how condensation processes directly enhance PV through the coupling of moisture, diabatic heating, and circulation dynamics under future warming scenarios (Eq. 36). The spatial heterogeneity, with drying tendencies over the North Atlantic sector in higher emission scenarios, illustrates the nonlinear redistribution of moisture by altered storm tracks and blocking patterns, consistent with the regime transition discussed in the 'A dynamical phase space for regime transition in Arctic amplification' section. These precipitation changes have profound implications for diabatic PV generation: enhanced latent heat release during condensation acts as a direct source of cyclonic PV anomalies in the lower troposphere (Eq. 34), reinforcing the positive feedback loop that accelerates Arctic amplification.

Nonlinear amplitude dynamics and subcritical instability

The transition from linear to nonlinear regimes identified in the phase space of Fig. 2 has profound implications for the temporal evolution of wave amplitudes. To understand how nonlinearity saturates–or, conversely, amplifies–wave growth under different values of the nonlinearity ratio $\mathcal{R}$, we turn to the Landau equation, which emerges from a weakly nonlinear expansion of the quasi-geostrophic PV equation (see the 'Nonlinear PV dynamics and Landau equation' subsection in 'Methods' for the full derivation). This amplitude equation captures the essential competition between linear growth and nonlinear feedback, and provides a conceptual bridge between the steady-state regime diagram and the transient dynamics that govern individual wave events. The Landau equation takes the form

$$\frac{dA}{dt} = \sigma_L A - \gamma |A|^2 A, \tag{1}$$

where A represents the complex amplitude of the most unstable linear mode, σ_L its linear growth rate, and γ the nonlinear coefficient that encodes the effect of wave-mean flow interactions and the stability feedback σ'. The sign of γ is critical: for $\gamma > 0$, the nonlinear term opposes the linear growth, leading to saturation at a finite equilibrium amplitude $A_\infty = \sqrt{\sigma_L/\gamma}$, a behaviour known as supercritical bifurcation. For $\gamma < 0$, however, the nonlinear term reinforces the linear growth, producing finite-time blow-up whenever the initial amplitude exceeds a threshold. This is the hallmark of subcritical instability: even when the basic state is linearly stable ($\sigma_L < 0$), a sufficiently large finite-amplitude perturbation can trigger explosive growth.

Our scaling analysis (the 'Nonlinear PV dynamics and Landau equation' subsection) shows that γ is controlled by the nonlinearity ratio $\mathcal{R} = |\sigma'/\overline{\sigma}|$ according to $\gamma \approx \gamma_0(\mathcal{C}_{\text{mean}} - \chi\mathcal{R})$, with $\chi \approx 3 - 4$ arising from the enhanced vertical curvature of Arctic eigenmodes under bottom-heavy warming. Consequently, γ changes sign when $\mathcal{R}$ exceeds a critical value $\mathcal{R}_c \approx 0.3$. For $\mathcal{R} < 0.3$ the dynamics are supercritical and waves saturate; for $\mathcal{R} > 0.3$ the system enters the subcritical regime, where finite-amplitude perturbations can grow explosively even if the linear growth rate is weak. Notably, the CMIP6 historical ensemble has a mean $\mathcal{R} \approx 0.4$ and a median of 0.38, with 67% of models exceeding $\mathcal{R}_c$. This conclusion is supported by the multi-model regime diagram (Fig. 2), the robust decrease in K_s^2 (Fig. 4), and the Landau analysis itself (Fig. 7). Thus, the Arctic atmosphere is already preconditioned for subcritical instability; the warming-induced increase in $\mathcal{D}$ provides the diabatic energy that allows this instability to be realised more frequently and intensely.

Figure 7 illustrates these different dynamical regimes through numerical solutions of the Landau equation. The parameters have been chosen to illustrate the qualitative behaviour of the Landau equation in a regime relevant to Arctic amplification. The linear growth rate $\sigma_L = 0.3\ \mathrm{day}^{-1}$ is consistent with the range of dry Eady growth rates diagnosed from CMIP6 models (approximately 0.28–0.31 day^{-1}; Fig. 3a). The nonlinear coefficient γ is taken as $10^{-6}\ \mathrm{s}^{-1}$, which yields a saturation amplitude $A_\infty = \sqrt{\sigma_L/\gamma}$ of order unity for the supercritical case and a threshold amplitude $A_c = \sqrt{|\sigma_L|/|\gamma|}$ of similar magnitude for the subcritical case-values that are plausible for large-scale atmospheric waves. Panel (a) shows the sensitivity to the linear growth rate σ_L for a fixed positive γ: larger growth rates produce faster saturation and higher equilibrium amplitudes. Panel (b) demonstrates the crucial role of the sign of γ: for $\gamma > 0$ the amplitude saturates; for $\gamma = 0$ it grows linearly without bound; and for $\gamma < 0$ it exhibits finite-time blow-up, the signature of subcritical instability. Panel (c) presents the corresponding phase portraits, highlighting the bifurcation structure: when $\gamma > 0$ a pair of stable fixed points appears (supercritical bifurcation); when $\gamma < 0$, these fixed points vanish, and all trajectories with sufficiently large initial amplitude diverge. Panel (d) focuses on the subcritical regime ($\gamma = -1 \times 10^{-6}\ \mathrm{s}^{-1}$) and reveals the threshold behaviour that is central to our interpretation of Arctic amplification. Only amplitudes above a critical value $A_c = \sqrt{|\sigma_L|/|\gamma|}$ trigger explosive growth; smaller disturbances decay. This threshold behaviour mirrors precisely the condition $\mathcal{R} > 0.3$ derived from our scaling analysis, confirming that when the nonlinear stability perturbation ratio exceeds this critical value, the system transitions from a damped to an amplified wave regime. The positive feedback loop (surface warming → reduced static stability → enhanced PV inversion efficiency → amplified streamfunction anomalies → increased poleward heat transport → further surface warming) is central to Arctic amplification. A linear stability analysis of a reduced coupled system representing this loop (see the 'Nonlinear PV dynamics and Landau equation' subsection in 'Methods') indicates that the loop is linearly unstable under plausible Arctic parameters, meaning that infinitesimal perturbations would grow exponentially in the absence of nonlinear effects. However, such exponential growth is not sustained; it is ultimately arrested by nonlinear saturation. Within the Landau framework (Eq. 16), the nonlinear term $-\gamma|A|^2 A$ counteracts linear growth when $\gamma > 0$, leading to a finite equilibrium amplitude (supercritical bifurcation). For $\gamma < 0$ (subcritical regime, $\mathcal{R} > 0.3$), the nonlinear term reinforces growth, but the system then undergoes explosive growth that is limited by other physical constraints or by the transition to a different dynamical regime. Thus, the loop gain estimate represents a theoretical possibility based on linearised scaling arguments, not a validated quantitative prediction, and the eventual arrest of growth is a direct consequence of the nonlinear PV-stability feedbacks captured by the Landau equation.

The relevance of this result for Arctic amplification is twofold. First, it provides a mechanistic explanation for the observed explosive growth of planetary waves prior to SSW events[26,31]: in the subcritical regime ($\mathcal{R} > 0.3$), a modest increase in wave amplitude above the threshold can trigger runaway growth, rapidly depositing momentum and heat into the stratosphere and decelerating the polar night jet. Second, it establishes a direct link between the steady-state regime diagram (Fig. 2) and the transient dynamics of extreme events. The moist-nonlinear quadrant of the phase space corresponds to the parameter region where $\mathcal{R} > 0.3$ and $\mathcal{D} > 0.03$; while the former condition is already satisfied historically, the latter is reached only under warming. Thus, as the Arctic trajectory moves vertically into the moist-nonlinear quadrant (Fig. 2), we expect not only a statistical increase in SSWs but also a qualitative change in their dynamics: they should become more explosive and more sensitive to the precise amplitude of the triggering wave. The framework offers a potential explanation for the dynamics of such extreme events, for example, the 2023/24 double-SSW event[32]. The Landau framework, therefore, serves as a dynamical backbone for understanding how the nonlinear regime transitions identified in this work manifest in the real atmosphere.

Discussion

We have developed a unified dynamical framework that reinterprets Arctic amplification as an emergent property of nonlinear PV dynamics, coupled with thermodynamic feedbacks and stratosphere-troposphere interactions. The cornerstone of this framework is the regime diagram (Fig. 2), which organises the Arctic atmosphere into four dynamical quadrants defined by two physically grounded dimensionless parameters: the nonlinearity ratio $\mathcal{R} = |\sigma'/\overline{\sigma}|$ and the diabatic number $\mathcal{D}$. This phase space provides a novel lens through which to understand the observed intensification of extreme weather, the increased frequency of SSWs, and the evolving connectivity between the Arctic and midlatitudes.

The key results of our study can be synthesised into three interconnected findings. First, the multi-model analysis of CMIP6 projections reveals that the historical Arctic resides in a dry-nonlinear state ($\mathcal{R} \approx 0.4$, $\mathcal{D} \approx 0.02$), with 67% of models already exceeding the $\mathcal{R} = 0.3$ threshold for subcritical instability. Under continued warming, the system migrates vertically into a moist-nonlinear regime ($\mathcal{D} > 0.03$), while $\mathcal{R}$ remaining essentially unchanged. This transition is driven by a robust increase in diabatic PV generation, as measured by $\mathcal{D}$ (100% of models show positive change, $p < 10^{-10}$), and represents a qualitative shift from dry baroclinic to moist diabatic dominance. Second, the dry Eady growth rate declines by approximately 9% under high-emission scenarios, yet this reduction is increasingly compensated by latent heat release, as evidenced by the systematic increase in the moist enhancement factor $\mathcal{F}$ (Fig. 3). While the absolute change in $\mathcal{F}$ is modest (~1%), it is statistically robust and consistent with Clausius-Clapeyron scaling, supporting the interpretation that moist processes are becoming more important. However, it is the increase in $\mathcal{D}$ that marks the qualitative shift to a moist-dominated regime. Third, the stationary wave refractive index K_s^2 exhibits a robust decrease across the CMIP6 ensemble (Fig. 4), consistent with the weakening of upper-level zonal winds due to reduced meridional temperature gradients. This pathway provides a mechanistic link between Arctic amplification and the observed increase in SSW frequency since 2000[23,26,27], independent of changes in $\mathcal{R}$.

Observational support for this dynamical reorganisation is provided by ERA5 reanalysis (Fig. 6), which reveals a striking vertical contrast in PV anomalies: strong positive anomalies dominate the lower troposphere over Arctic oceanic regions, consistent with enhanced latent heating, while the upper troposphere exhibits wave-like patterns indicative of altered Rossby wave guidance. This vertical contrast is qualitatively consistent with the conceptual illustration provided by the mcTRSW model (the 'Condensation-driven PV dynamics: insights from the mcTRSW model' subsection in 'Methods'), which shows how condensation can generate a PV contrast in a simplified setting. The consistency between theory, models, and observations strengthens the case that Arctic amplification is not merely a passive thermodynamic response but an active dynamical process that fundamentally reorganises the large-scale circulation.

The critical thresholds identified in this study, $\mathcal{R}_c \approx 0.3$ for the onset of subcritical instability and $\mathcal{D}_c \approx 0.03$ for the transition to diabatic dominance, offer quantitative benchmarks for monitoring the evolving Arctic system. These thresholds are not arbitrary but emerge from the competition between stabilising mean-flow feedbacks and destabilising stability feedbacks in the Landau coefficient (the 'Nonlinear PV dynamics and Landau equation' subsection in 'Methods'). The Landau framework further illustrates that for $\mathcal{R} > 0.3$, the system enters a subcritical instability regime where finite-amplitude perturbations can grow explosively even when the linear growth rate is weak (Fig. 7). Because this condition is already met in the historical climate, the increase in $\mathcal{D}$ under warming provides the diabatic energy that enables this instability to be realised more frequently and intensely. The projected reduction in lower-tropospheric static stability (Fig. 2) amplifies baroclinic growth rates (Fig. 3) and enhances diabatic heating from latent heat release, together leading to larger-amplitude tropospheric waves. These waves carry increased upward wave activity flux into the stratosphere, favouring more frequent SSWs. However, the long-term stratospheric cooling (Fig. 5b) strengthens the mean polar vortex, which would oppose SSW occurrence. The net response of SSW frequency to increasing radiative forcing thus depends on the competition between enhanced upward wave driving (favouring more SSWs) and a stronger, more resilient vortex (favouring fewer SSWs). A multi-model assessment[33] found no statistically significant future change in SSW frequency, consistent with the idea that these opposing effects may cancel.

Three novel contributions distinguish our framework from previous studies. First, the $\mathcal{R}$-$\mathcal{D}$ phase space (Fig. 2) provides a two-dimensional classification of Arctic dynamics—a -regional division- into four quadrants based on objective dimensionless parameters, enabling identification of qualitative regime transitions rather than gradual trends. Second, the Landau analysis yields the first quantitative threshold $\mathcal{R}_c = 0.3$ for the onset of subcritical instability in the Arctic, extending classical baroclinic instability theory to the nonlinear regime. Third, the K_s^2 diagnostic (Eq. 10) quantitatively connects surface-driven static stability changes to stratospheric wave propagation, providing a mechanistic link for stratosphere-troposphere coupling. Unlike previous studies that emphasised thermodynamic feedbacks or observational pattern recognition (e.g. ref. 18), our framework highlights nonlinear PV dynamics and wave-mean flow interactions as an organising principle.

Our findings have implications for climate modelling and prediction. The narrowing of inter-model spread in the moist enhancement factor $\mathcal{F}$ under stronger forcing (Fig. 3b) indicates that the thermodynamic response to warming (Clausius-Clapeyron scaling) is more robustly captured across models than the dynamical changes in dry baroclinicity. This suggests that model projections of future storm tracks and blocking frequencies may be more sensitive to the representation of moisture-dynamics coupling than to the precise magnitude of dry baroclinic weakening. Consequently, traditional diagnostics based solely on cyclone counts or dry Eady growth rates may underestimate the true extent of dynamical change. Instead, metrics that capture the amplitude and persistence of PV anomalies, vertically integrated eddy kinetic energy, diabatic heating rates, and crucially, the diabatic number $\mathcal{D}$ itself, will be essential for monitoring and projecting climate variability in a warming world.

Several limitations of this study warrant acknowledgement. A fully rigorous demonstration of subcritical instability would require numerical continuation of the full primitive equation system, which lies beyond the present scope. Likewise, the ageostrophic corrections estimated in 'Methods' rely on scaling arguments that should be verified with high-resolution simulations that explicitly resolve moist processes and boundary layer dynamics. The simplified Eady model, while capturing the essential competition between dry and moist processes, omits the effects of vertical wind shear variations and the detailed structure of diabatic heating profiles. Future work should address these limitations through idealised numerical experiments and through the analysis of convection-permitting simulations that can better represent the small-scale processes underlying diabatic PV generation.

Despite these caveats, the coherence of the multi-model evidence, the consistency with observational data, and the qualitative agreement with theoretical predictions provide strong support for the proposed dynamical pathway. The regime diagram presented here offers a unifying framework for interpreting a wide range of phenomena, from storm intensification and blocking persistence to SSWs and Arctic-midlatitude teleconnections, as manifestations of a fundamental reorganisation of atmospheric dynamics under polar amplification. By identifying the critical thresholds that govern this reorganisation, our work provides testable hypotheses for future observational and modelling studies and offers quantitative targets for evaluating and improving climate model projections.

Ultimately, polar amplification represents more than a simple thermodynamic response to radiative forcing; it is a harbinger of a planetary-scale dynamical transition. The Arctic is entering a regime where nonlinearity and diabatic processes dominate, with consequences that extend far beyond the high latitudes. Improving the representation of the interconnected processes identified in this study—nonlinear PV dynamics, static stability feedbacks, diabatic PV generation, and stratosphere-troposphere coupling—is crucial for reducing uncertainty in projections of both polar and midlatitude climate and for developing accurate assessments of regional climate impacts associated with continued Arctic warming.

Methods

Data and preprocessing

We analyse 38 CMIP6 models from the historical experiment (1980–2000) and two Shared Socioeconomic Pathway scenarios: SSP2-4.5 and SSP5-8.5, each evaluated at mid-century (2040–2060) and end-century (2080–2100) windows. Monthly mean fields of air temperature (*ta*), zonal and meridional wind (*ua*, *va*), and specific humidity (*hus*) are retrieved on native model grids and regridded to a common 2° × 2° latitude-longitude grid using bilinear interpolation. All fields are annual means for each model and period; no seasonal filtering is applied. Quality filters exclude MCM-UA-1-0 (corrupt pressure-level data) from all diagnostics and MPI-ESM1-2-HR from wave diagnostics due to an anomalous historical deformation radius (~50 km vs ensemble mean ~375 km). Observational baselines are provided by ERA5[34] and NCEP/NCAR Reanalysis 1, each evaluated over three overlapping 30-year windows (1961–1990, 1981–2010, 1991–2020) to characterise internal variability.

Statistical testing

Paired percentage changes (future minus historical, per model) are assessed using the Wilcoxon signed-rank test with the null hypothesis that the median change equals zero. Significance levels are denoted $p < 0.05$, $p < 0.01$, $p < 0.001$. Cross-model relationships are quantified using Pearson correlation with associated p-values from a two-tailed t-test; ordinary least-squares regression lines are computed on pooled scenario-period data.

Quasi-geostrophic PV formulation

The QG pseudo-PV in pressure coordinates (x, y, p) is given by refs.[35,36]:

$$q_p = \nabla^2\psi + f_0^2 \frac{\partial}{\partial p}\left(\frac{1}{\bar{\sigma}(p)}\frac{\partial\psi}{\partial p}\right) + \beta y, \tag{2}$$

where $\psi = \varphi/f_0$ is the geostrophic streamfunction, φ the geopotential, f_0 the reference Coriolis parameter, and $\bar{\sigma}(p)$ the background static stability. Following Holton [37], static stability is defined as

$$\sigma(p) = -\frac{RT}{p\theta}\frac{\partial\theta}{\partial p}, \tag{3}$$

with units $m^2\,s^{-2}\,Pa^{-2}$. This formulation captures ~85–90% of PV variability at synoptic scales in the Arctic tropopause region[38].

Nonlinearity ratio and diabatic number

The nonlinearity ratio $\mathcal{R} = \langle|\sigma'|\rangle/\bar{\sigma}$ is computed from the static stability parameter $\sigma(p)$ defined in Eq. (3). The background stability $\bar{\sigma}$ and perturbation magnitude $\langle|\sigma'|\rangle$ are obtained as pressure-weighted vertical averages over the 500–850 hPa layer and area-weighted spatial averages over the 60–90° N polar cap. This ratio directly compares the magnitude of stability perturbations induced by warming to the climatological background stability; values exceeding 0.3 indicate that nonlinear effects dominate the PV dynamics (see scaling analysis below).

The diabatic number $\mathcal{D}$ is defined as the ratio of diabatic PV generation to baroclinic advection:

$$\mathcal{D} = \frac{\left|q'\frac{f+\zeta}{\theta}\left(\frac{L_v}{c_p\Pi}\frac{Dr_v}{Dt}\right)'\right|}{|q'\mathbf{v}'\cdot\nabla\bar{q}|}. \tag{4}$$

For practical computation from climate model output, we employ a column-integrated scaling form:

$$\mathcal{D} = \frac{L_v\bar{P}}{c_p\,|\partial T/\partial y|\,f_0\,L_d\,H}, \tag{5}$$

where $\bar{P}$ is the domain-mean precipitation rate (representing the net latent heating), $|\partial T/\partial y|$ is the 500 hPa meridional temperature gradient between 40–60° N and 60–80° N, L_d is the Rossby deformation radius, and H is the pressure scale height. This formulation captures the essential competition between diabatic heating and baroclinic eddy generation.

The threshold values $\mathcal{R}_c = 0.3$ and $\mathcal{D}_c = 0.03$ are derived from scaling analysis of the eddy PV variance equation (see the 'Nonlinear PV dynamics and Landau equation' subsection below). $\mathcal{R}_c$ corresponds to the point where the destabilising stability feedback overcomes the stabilising mean-flow feedback in the Landau coefficient, while $\mathcal{D}_c$ marks the transition where diabatic PV generation becomes comparable to baroclinic production. These thresholds are consistent with observed climatological values and with the systematic model shifts evident in Fig. 2.

Bifurcation framework for regime transition

A minimal conceptual model for the transition between dry and moist regimes is provided by a Landau-type potential for an order parameter ψ (e.g. eddy kinetic energy or diabatic heating rate):

$$V(\psi) = -\frac{1}{2}\mu(\Delta T, q)\,\psi^2 + \frac{1}{4}\lambda\psi^4, \tag{6}$$

where $\mu = \alpha\Delta T + \beta q - \mu_c$ measures the distance from criticality, with $\alpha \approx 0.15\ K^{-1}$ and $\beta \approx 0.3\ kg^{-1}\ m^2$ estimated from reanalysis composites, and $\lambda > 0$. The critical threshold μ_c separates the dry ($\mu < 0$) and moist ($\mu > 0$) regimes. This bifurcation structure underlies the regime diagram of Fig. 2, with $\mathcal{R}$ and $\mathcal{D}$ acting as observable proxies for the control parameters.

Eady growth rate diagnostics

The dry Eady growth rate is computed as $\sigma_E = 0.31\ (f/N)\ |\partial u/\partial z|$, where the Brunt-Väisälä frequency N and vertical wind shear $|\partial u/\partial z|$ are evaluated as pressure-weighted averages over the 500–850 hPa layer and area-weighted averages over 50–70° N. A floor of $N_{\min} = 5\times10^{-4}\ s^{-1}$ is applied to prevent division by zero at weakly stable grid points. To account for the reduction of effective stratification by latent heat release in saturated ascent, the moist Eady growth rate is obtained by replacing the dry static stability with moist static stability. Following the modified Eady model[35,39], the moist Eady growth rate can be approximated as

$$\sigma_{E,\mathrm{moist}} = \sigma_E \times \mathcal{F}(\mathrm{RH}, T), \tag{7}$$

with the enhancement factor

$$\mathcal{F}(\mathrm{RH},\mathrm{T}) = 1 + \frac{\mathrm{L_v q_s}}{\mathrm{c_p T}}\left(\frac{\mathrm{RH}}{100}\right)^{\gamma}, \tag{8}$$

where q_s is the saturation specific humidity, RH the relative humidity, and $\gamma \approx 0.5$–0.8 an empirical exponent. This expression arises from linearising the thermodynamic equation, including latent heating and reflects Clausius-Clapeyron scaling (a detailed derivation is given in the Supplementary Information). The moist enhancement factor is then defined as $F = \sigma_{E,\mathrm{moist}}/\sigma_{E,\mathrm{dry}}$. Domain-mean values of σ_E, $\sigma_{E,\mathrm{moist}}$, and F are computed for each model, scenario and time period. Models with $\mathcal{R} > 1.5$ or $\sigma_{E,\mathrm{dry}} < 0.01\ \mathrm{day}^{-1}$ are excluded as unphysical outliers.

Wave diagnostics

The Rossby deformation radius is computed as $L_d = NH/(f_0\pi)$, where N is the domain-mean Brunt–Väisälä frequency over 500–850 hPa and 55–75° N, H is the scale height, and f_0 is the Coriolis parameter at 65° N. The stationary wavenumber squared is computed as $K_s^2 = \beta^*/\overline{u}_M$ at 250 hPa over 50–70° N, where $\overline{u}_M$ is the zonal-mean zonal wind and the meridional gradient of absolute vorticity is computed with the full spherical metric:

$$\beta^* = \frac{2\Omega\cos\varphi}{a} - \frac{1}{a^2\cos\varphi}\frac{d}{d\varphi}\left(\cos\varphi\frac{d\bar{u}}{d\varphi}\right). \tag{9}$$

Percentage changes in L_d and K_s^2 are computed relative to each model's own historical-period value.

Theoretical framework for refractive index modification under Arctic amplification. The refractive index squared for stationary Rossby waves in the log-pressure coordinate formulation is given by ref.[29]:

$$n^2(z) = \frac{\overline{q}_y}{\overline{u}} - k^2 - \frac{f_0^2}{4N^2H^2}, \tag{10}$$

where $\overline{q}_y = \partial\overline{q}/\partial y$ is the meridional gradient of PV, $\overline{u}$ the zonal-mean zonal wind, k the zonal wavenumber, N the buoyancy frequency, and H the scale height. Vertical propagation occurs where $n^2 > 0$; waves are evanescent where $n^2 < 0$.

Under Arctic amplification, the dominant modification to n^2 is the weakening of $\overline{u}$ due to reduced meridional temperature gradients, which decreases the denominator in the first term and thus reduces $K_s^2 = n^2 + k^2$. This thermal-wind response is a robust feature across CMIP6 models and provides a direct mechanistic link between surface warming and enhanced vertical wave penetration. Changes in static stability (quantified by $\mathcal{R}$) can, in principle, modulate $\overline{q}_y$ through nonlinear terms, but in the CMIP6 ensemble, this effect is secondary to the robust thermal-wind response. The refractive index decrease is therefore interpreted primarily as a consequence of the thermodynamic response to warming, independent of the precise value of $\mathcal{R}$.

Nonlinear PV dynamics and Landau equation

Nonlinear perturbation PV equation. To capture leading-order nonlinear effects, we introduce a small perturbation to the relevant fields as $\overline{\sigma}(p) + \sigma'(x, y, p, t)$, $\psi = \psi'(x, y, p, t)$ (with background streamfunction taken as zero), and $q_p = \beta y + q_p'$. Expanding the inverse of static stability to first order and substituting into the QG PV equation yields the nonlinear form of the perturbation PV equation:

$$q_p' = \nabla^2\psi' + f_0^2\frac{\partial}{\partial p}\left(\frac{1}{\overline{\sigma}}\frac{\partial\psi'}{\partial p}\right) - f_0^2\frac{\partial}{\partial p}\left(\frac{\sigma'}{\overline{\sigma}^2}\frac{\partial\psi'}{\partial p}\right). \tag{11}$$

The first two terms constitute the linear QG PV operator applied to ψ', while the third term represents a feedback where static stability perturbations (σ') modulate PV inversion efficiency through nonlinear coupling. This mechanism exhibits particular potency in the Arctic due to the climatologically weak background stability and the amplified magnitude of warming-induced stability perturbations.

Relation between stability perturbations and flow curvature. Using the hydrostatic relation and the definition of static stability, one can derive that the stability perturbation is proportional to the vertical curvature of the streamfunction:

$$\sigma' \propto \frac{\partial^2\psi'}{\partial p^2}, \tag{12}$$

where the proportionality factor depends on background state variables. The sign of σ' is controlled by the vertical curvature of ψ': a concave-up profile $(\partial^2\psi'/\partial p^2 > 0)$ implies $\sigma' > 0$ (increased stability), whereas a concave-down profile $(\partial^2\psi'/\partial p^2 < 0)$ implies $\sigma' < 0$ (destabilisation). Under typical Arctic conditions, where $\partial\psi'/\partial p < 0$, the nonlinear PV equation implies that warming reduces static stability ($\sigma' < 0$), which weakens the polar vortex and enhances wave activity.

Nonlinear timescale and comparison with advective processes. Scaling the nonlinear term in Eq. (11) as $N_{\text{nonlinear}} \sim f_0^2\mathcal{R}\psi_0'/(\overline{\sigma}\Delta p^2)$ and the linear PV tendency as $\partial q_p'/\partial t \sim \omega q_p' \sim \omega f_0^2\psi_0'/(\overline{\sigma}\Delta p^2)$ yields a nonlinear timescale

$$\tau_{\text{nonlinear}} \sim \frac{1}{\mathcal{R}\omega} \sim \frac{\tau_{\text{wave}}}{\mathcal{R}}, \tag{13}$$

indicating that nonlinear effects accumulate over multiple wave cycles. Comparing the nonlinear term with advective processes gives a nonlinearity parameter $\mathcal{N} \sim \mathcal{R}\cdot\text{Ro}^{-1}$, where Ro = $U/(f_0L)$ is the Rossby number. For Arctic conditions (Ro ~ 0.1, $\mathcal{R} \sim 0.2$), $\mathcal{N} \sim 2$, indicating that nonlinear stability effects become comparable to or exceed advective processes.

Dimensionless parameter hierarchy and composite interaction parameter. The dynamics are governed by a hierarchy of dimensionless parameters: Rossby number Ro ~ 0.1, Froude number Fr ~ 0.3, nonlinearity ratio $\mathcal{R} \sim 0.2$, and baroclinicity parameter $\mathcal{B} \sim 5$. A composite nonlinear interaction parameter $\mathcal{I} = \mathcal{R}\cdot\text{Ro}^{-1}\cdot\text{Fr}^{-1}$ measures the dominance of the nonlinear PV-stability feedback; for the Arctic, $\mathcal{I} \sim 6.7 > 1$, confirming the importance of nonlinear dynamical feedbacks.

Weakly nonlinear expansion and Landau equation. We perform a systematic weakly nonlinear expansion of Eq. (11) to derive an amplitude equation for the most unstable linear mode. Introducing a small parameter $\epsilon \ll 1$ and a slow time $T = \epsilon^2 t$, we write

$$\psi' = \epsilon\psi_1 + \epsilon^2\psi_2 + \epsilon^3\psi_3 + \cdots, \ \sigma' = \epsilon\sigma_1 + \epsilon^2\sigma_2 + \epsilon^3\sigma_3 + \cdots, \tag{14}$$

with $\sigma_n \propto \partial^2\psi_n/\partial p^2$. At $\mathcal{O}(\epsilon)$ we obtain the linear eigenvalue problem $\mathcal{L}\psi_1 = 0$ with solution

$$\psi_1 = A(T)\,\phi(y, p)\,e^{i(kx-\omega t)} + \text{c.c.}, \tag{15}$$

where ϕ is the eigenfunction and $\sigma_L = \text{Im}(\omega)$ the linear growth rate. At $\mathcal{O}(\epsilon^2)$, quadratic interactions force a mean-flow correction $\overline{\psi}_2$ and a second harmonic $\psi_2^{(2)}$. At $\mathcal{O}(\epsilon^3)$, a solvability condition yields the Landau equation

$$\frac{dA}{dt} = \sigma_L A - \gamma|A|^2 A, \tag{16}$$

where the nonlinear coefficient γ is given by an integral involving the eigenfunction, the adjoint, and the second-order fields.

Scaling estimate for the critical threshold $\mathcal{R}_c$. The numerator of γ contains two competing contributions: a mean-flow feedback (typically stabilising, $\propto \mathcal{C}_{\text{mean}}$) and a stability feedback (destabilising, $\propto \chi\mathcal{R}$), where $\chi \approx 3-4$ arises from the enhanced vertical curvature of the eigenmode under bottom-heavy Arctic warming. Balancing these gives $\gamma \approx \gamma_0(\mathcal{C}_{\text{mean}} - \chi\mathcal{R})$. Thus, γ changes sign when $\chi\mathcal{R} \gtrsim \mathcal{C}_{\text{mean}}$. With $\mathcal{C}_{\text{mean}} \sim 0.5 - 1.5$ and χ ~ $3-4$, the critical nonlinearity ratio satisfies

$$\mathcal{R}_c \approx \frac{\mathcal{C}_{\text{mean}}}{\chi} \approx 0.12 - 0.5, \tag{17}$$

and we adopt a conservative value $\mathcal{R}_c \approx 0.3$, consistent with observational and model data (Fig. 2). This threshold marks the transition to subcritical instability, where $\gamma < 0$ enables explosive wave growth even when $\sigma_L < 0$.

Bifurcation structure and subcritical instability. For $\gamma > 0$, the Landau equation has a stable finite-amplitude equilibrium at $|A| = \sqrt{\sigma_L/\gamma}$ when $\sigma_L > 0$ (supercritical bifurcation). For $\gamma < 0$, the equation becomes

$$\frac{dA}{dt} = \sigma_L A + |\gamma||A|^2 A, \tag{18}$$

which exhibits finite-time blow-up for any initial condition when $\sigma_L > 0$. When $\sigma_L < 0$, the origin is linearly stable, but perturbations with $|A| > \sqrt{|\sigma_L|/|\gamma|}$ experience unbounded growth, the hallmark of subcritical instability. The threshold amplitude $A_c = \sqrt{|\sigma_L|/|\gamma|}$ defines a separatrix. Under Arctic conditions with $\mathcal{R} > 0.3$, our scaling estimate yields $\gamma < 0$, implying that such a subcritical bifurcation structure may be realised, consistent with the explosive growth observed in SSW events.

Lapse rate feedback and static stability

Lapse rate definition and linearization. The lapse rate $\Gamma = -\partial T/\partial z$ combines the dry adiabatic gradient and the stability-dependent component:

$$\Gamma \equiv -\frac{\partial T}{\partial z} = \frac{g}{c_p} + \frac{T}{\theta}\frac{\partial \theta}{\partial z} = \frac{g}{c_p}(1 + \frac{R}{c_p}\frac{\partial \ln\theta}{\partial \ln p}). \tag{19}$$

Linearising about a background state yields the scaling for the lapse rate anomaly:

$$\Gamma' \sim \frac{g}{c_p}\frac{\sigma'}{\bar{\sigma}}\left[1 - \frac{1}{2}\left(\frac{\theta'}{\bar{\theta}}\right) + \mathcal{O}\left(\frac{\theta'}{\bar{\theta}}\right)^2\right], \tag{20}$$

where the relationship $\sigma' \propto \partial^2\psi'/\partial p^2$ has been incorporated.

Moist thermodynamic framework. Within moist thermodynamics, the relevant conserved quantity is the moist static energy $h = c_pT + gz + L_v q_v$. The moist adiabatic lapse rate Γ_m deviates from the dry adiabatic lapse rate $\Gamma_d = g/c_p$ due to latent heat release:

$$\Gamma_m = \Gamma_d \frac{1 + \frac{L_v q_v}{R_d T}}{1 + \frac{\epsilon L_v^2 q_v}{c_p R_v T^2}}, \tag{21}$$

where $\epsilon = R_d/R_v \approx 0.622$. Differentiating with respect to specific humidity shows $\partial\Gamma_m/\partial q_v < 0$ for all tropospheric temperatures, i.e. the moist adiabatic lapse rate decreases monotonically with increasing specific humidity.

Boundary layer and convective instability. In a convective equilibrium framework, the net radiative cooling $Q_{\rm rad} \sim 1 - 2\,{\rm K\,day^{-1}}$ must be balanced by convective heating when the lapse rate exceeds a critical value. The onset of convection follows from the moist Brunt-Väisälä frequency:

$$N_m^2 = \frac{g}{\theta_v}\frac{\partial\theta_v}{\partial z} = \frac{g}{T}\left(\frac{\partial T}{\partial z} + \Gamma_d - \frac{L_v}{c_p}\frac{\partial q_v}{\partial z}\right), \tag{22}$$

with θ_v the virtual potential temperature. Convection occurs when $N_m^2 < 0$, yielding a critical stability threshold

$$\sigma' < \sigma_{\rm crit} = \bar{\sigma}\left[1 - \frac{R}{g}\left(\Gamma_d - \frac{L_v}{c_p}\frac{\partial q_v}{\partial z}\right)T\right]. \tag{23}$$

For typical Arctic conditions ($RH \sim 80\%$, $T \sim 260$ K), $\sigma_{\rm crit} \sim 0.7\bar{\sigma}$. As warming reduces $\bar{\sigma}$ and increases q_v, $\sigma_{\rm crit}$ decreases, making convection more likely and creating a positive feedback.

Vertical structure and Sturm–Liouville analysis. The linearised thermodynamic equation with variable static stability leads to a Sturm–Liouville eigenvalue problem:

$$\frac{\partial}{\partial p}\left(\frac{f_0^2}{\sigma(p)}\frac{\partial\varphi'}{\partial p}\right) + \lambda\varphi' = 0, \tag{24}$$

where λ is the eigenvalue. The eigenfunctions $\phi_n(p)$ form a complete orthogonal basis. Under polar amplification, $\sigma(p)$ decreases in the lower troposphere, shifting eigenvalues and increasing the amplitude of higher baroclinic modes ($n \geq 1$), explaining the observed surface-amplified warming structure. A 20% reduction in stability generates a lapse rate anomaly of $\Gamma\prime \sim -0.3\ {\rm K\,km^{-1}}$, which enhances near-surface warming, increases downward longwave radiation, and reduces the Rossby deformation radius.

Eddy PV variance equation

The eddy PV variance equation, which underpins the definition of the diabatic number $\mathcal{D}$ and the interpretation of the regime transition, is derived from the quasi-geostrophic PV equation including diabatic sources[16,35]:

$$\frac{Dq}{Dt} = \mathcal{S}, \tag{25}$$

where q is the QG PV, $D/Dt = \partial_t + \mathbf{v}_g\cdot\nabla$ is the material derivative following the geostrophic flow, and $\mathcal{S}$ represents diabatic and frictional sources. Decomposing fields into a background state (denoted by an overbar) and a perturbation (denoted by a prime) as $q = \overline{q} + q'$, $\mathbf{v}_g = \overline{\mathbf{v}}_g + \mathbf{v}_g'$, and $\mathcal{S} = \overline{\mathcal{S}} + \mathcal{S}'$, and subtracting the mean state, yields the perturbation PV equation:

$$\frac{\partial q'}{\partial t} + \overline{\mathbf{v}}_g\cdot\nabla q' + \mathbf{v}_g'\cdot\nabla\overline{q} + \mathbf{v}_g'\cdot\nabla q' - \overline{\mathbf{v}_g'\cdot\nabla q'} = \mathcal{S}'. \tag{26}$$

Multiplying by q' and averaging gives the eddy PV variance equation:

$$\frac{\partial}{\partial t}(\frac{\overline{q'^2}}{2}) + \overline{\mathbf{v}}_g\cdot\nabla(\frac{\overline{q'^2}}{2}) = -\overline{q'\mathbf{v}_g'}\cdot\nabla\overline{q} + \overline{q'\mathcal{N}'} + \overline{q'\mathcal{S}'}, \tag{27}$$

where $\mathcal{N}' = \mathbf{v}_g'\cdot\nabla q' - \overline{\mathbf{v}_g'\cdot\nabla q'}$ represents nonlinear eddy–eddy interactions. The term $-\overline{q'\mathbf{v}_g'}\cdot\nabla\overline{q}$ is the baroclinic production rate, while $\overline{q'\mathcal{S}'}$ represents diabatic generation or dissipation.

For Arctic amplification, the dominant diabatic process is latent heat release. Following Hoskins et al. [16], the diabatic PV tendency can be expressed in terms of the diabatic heating rate $\dot{\theta}$:

$$\mathcal{S} = \frac{f+\zeta}{\theta}\frac{\partial\dot{\theta}}{\partial p} + {\rm frictionalterms}. \tag{28}$$

The diabatic heating rate is given by $\dot{\theta} = (p_0/p)^\kappa(L_v/c_p\Pi)(Dr_v/Dt) + {\rm radiativeterms}$, where $\kappa = R/c_p$, $\Pi = (p/p_0)^{R/c_p}$ is the Exner function, and Dr_v/Dt is the net condensation rate. Linearizing and retaining the latent heating contribution yields:

$$\mathcal{S}' \approx \frac{f+\zeta}{\theta}\frac{\partial}{\partial p}\left[\left(\frac{p_0}{p}\right)^\kappa\frac{L_v}{c_p\Pi}\left(\frac{Dr_v}{Dt}\right)'\right]. \tag{29}$$

For synoptic-scale eddies, the vertical derivative can be approximated by a finite difference over the depth of the heating layer. Assuming heating concentrated in the mid-troposphere (700–400 hPa) and that the vertical structure is dominated by the first baroclinic mode gives:

$$\mathcal{S}' \approx \frac{f+\zeta}{\theta} \cdot \frac{L_v}{c_p \Pi \, \Delta p} \left(\frac{Dr_v}{Dt} \right)', \tag{30}$$

where Δp is the pressure thickness of the heating layer. Substituting into the variance equation and focusing on the diabatic contribution yields:

$$\overline{q' \mathcal{S}'} = \overline{q' \frac{f+\zeta}{\theta} \left(\frac{L_v}{c_p \Pi} \frac{Dr_v}{Dt} \right)'}. \tag{31}$$

For the purposes of the main text, we drop the overbar notation for ensemble averages and absorb nonlinear transfers into the material derivative, yielding the compact form:

$$\frac{D}{Dt}\left(\frac{q'^2}{2}\right) = \underbrace{-q'\mathbf{v}' \cdot \nabla \bar{q}}_{\text{baroclinicproduction}} + \underbrace{q' \frac{f+\zeta}{\theta} \left(\frac{L_v}{c_p \Pi} \frac{Dr_v}{Dt} \right)'}_{\text{diabaticintensification}}. \tag{32}$$

This equation partitions eddy PV variance growth into baroclinic production and diabatic intensification, providing the theoretical foundation for the diabatic number $\mathcal{D}$ and the regime diagram of Fig. 2.

Ertel PV theorem and diabatic source. The material derivative of Ertel PV $q_{\text{Ertel}} = (\zeta + f)\sigma^{-1}$ (with $\sigma = -\partial\theta/\partial p$) is given by

$$\frac{Dq_{\text{Ertel}}}{Dt} = \frac{1}{\rho} (\nabla\theta \times \nabla \dot{\theta}) \cdot \mathbf{k} + \text{frictionalterms}, \tag{33}$$

where $\dot{\theta}$ is the diabatic heating rate[16]. For condensation heating, $\dot{\theta}$ is positive and has a strong vertical gradient in the lower troposphere. The cross product $\nabla\theta \times \nabla \dot{\theta}$ then generates a positive PV anomaly in the lower layer, directly linking latent heat release to PV production. This term is the basis for the diabatic intensification in Eq. (32). A similar mechanism is explicitly represented in the moist-convective Thermal Rotating Shallow Water (mcTRSW) model (Eq. 36).

Parameterisation of diabatic PV generation. The diabatic PV tendency in the Arctic can be parameterised through an amplification factor that captures the nonlinear enhancement due to warming and sea ice loss:

$$\left(\frac{Dq}{Dt} \right)_{\text{diabatic}} = \mathcal{A}_{\text{Arctic}} \cdot \frac{f+\zeta}{\theta} \left[\frac{L_v}{c_p \Pi} \frac{Dr_v}{Dt} + \frac{L_s}{c_p \Pi} \frac{Dr_s}{Dt} \right], \tag{34}$$

with $\mathcal{A}_{\text{Arctic}} = 1 + \alpha(T - T_0) + \beta(\text{SIC}_0 - \text{SIC})$, where $\alpha \approx 0.07\ \text{K}^{-1}$ and $\beta \approx 0.02\ \%^{-1}$ are empirical coefficients derived from reanalysis composites. This parameterisation reflects the increased efficiency of diabatic PV generation under warmer and more ice-free conditions, and is used in the interpretation of projected precipitation changes (the 'Vertical structure of PV anomalies' section).

Condensation-driven PV dynamics: insights from the mcTRSW model

The mcTRSW model is used here as an idealised framework to illustrate the qualitative dynamics of condensation-induced PV contrast in the lower and upper layer[40–42]. This two-layer reduced model incorporates prognostic equations for layer thickness h_i, horizontal velocity $\mathbf{v}_i$, buoyancy b_i, and humidity q_i, offering a simplified tool for understanding the dynamical consequences of moist processes.

Condensation parameterization. Condensation is parameterised via a Betts–Miller-type relaxation scheme:

$$\mathcal{C} = \frac{q_1 - Q_s}{\tau_c} \mathbf{H}(q_1 - Q_s), \tag{35}$$

where τ_c is a relaxation timescale, Q_s the saturation value, and $\mathbf{H}$ the Heaviside step function. This formulation ensures that condensation occurs only when the lower-layer humidity exceeds saturation, releasing latent heat and modifying buoyancy.

PV evolution equation. The nondimensional PV evolution equation for each layer takes the form:

$$(\partial_t + \mathbf{v}_i \cdot \nabla)\mathbf{Q}_i = \frac{1}{h_i} \mathcal{J}(h_i, b_i) - \frac{1}{b_i} \mathbf{Q}_i \widetilde{\mathbf{z}}_i, \tag{36}$$

where $\mathbf{Q}_i$ is the PV in layer i, $\mathcal{J}$ is the Jacobian operator capturing nonlinear interactions between thickness and buoyancy fields, and $\widetilde{\mathbf{z}}_i$ encapsulates condensation and diabatic forcings.

Source terms and vertical structure. The source terms for the lower and upper layers are given explicitly by:

$$\widetilde{\mathbf{z}}_1 = (1-\gamma)(-\mathcal{C} + \mathcal{D}) - (1 - \gamma^F)\mathbf{F}_1, \tag{37}$$

$$\widetilde{\mathbf{z}}_2 = (1-\gamma)(\mathcal{C} - \mathcal{D}) - (1 - \gamma^F)\mathbf{F}_2, \tag{38}$$

where γ and γ^F are parameters regulating convective and external thermal forcing, $\mathbf{F}_i$ represents external heating, and downdrafts $\mathcal{D}$ ensure mass conservation. These expressions illustrate that condensation ($\mathcal{C}$) acts as a positive PV source in the lower troposphere and a sink in the upper layer, while downdrafts have the opposite effect.

This condensation-induced vertical PV contrast, positive anomalies at low levels and weaker anomalies aloft, is qualitatively similar to the vertical structure observed in ERA5 reanalysis (Fig. 6) and directly supports the diabatic intensification term in the eddy PV variance equation (Eq. 32). Even in the absence of potential temperature effects, a similar mechanism operates[43], demonstrating the robustness of condensation-driven PV source/sink behaviour. The mcTRSW model thus provides a conceptual illustration of how condensation processes can enhance PV through the coupling of moisture, diabatic heating, and circulation dynamics, a mechanism that becomes increasingly important under future warming scenarios.

Data availability

The CMIP6 model output used in this study is publicly available through the Earth System Grid Federation (ESGF; https://esgf-node.1lnl.gov/). ERA5 reanalysis data are available from the Copernicus Climate Data Store (https://cds.climate.copernicus.eu/). Processed diagnostic fields derived from these datasets are available from the corresponding author upon reasonable request.

Code availability

The analysis code used to produce the figures and diagnostics in this study is available on ZENODO at https://zenodo.org/records/20166650 and on GitHub at https://github.com/bijanf/arctic-regime-diagram.

Received: 3 March 2026; Accepted: 12 May 2026;
Published online: 25 May 2026

References

1. Screen, J. A. & Simmonds, I. The central role of diminishing sea ice in recent Arctic temperature amplification. *Nature* **464**, 1334–1337 (2010).

2. Pithan, F. & Mauritsen, T. Arctic amplification dominated by temperature feedbacks in contemporary climate models. *Nat. Geosci.* **7**, 181–184 (2014).
3. Francis, J. A., Vavrus, S. J. & Cohen, J. Amplified arctic warming and mid-latitude weather: new perspectives on emerging connections. *WIREs Clim. Change* **8**, e474 (2017).
4. Zhang, Y., Kong, Y., Yang, S. & Hu, X. Asymmetric Arctic and Antarctic warming and its intermodel spread in CMIP6. *J. Clim.* **36**, 8299–8310 (2023).
5. Rantanen, M. et al. The Arctic has warmed nearly four times faster than the globe since 1979. *Commun. Earth Environ.* **3**, 168 (2022).
6. Wendisch, M. et al. Atmospheric and surface processes, and feedback mechanisms determining Arctic amplification: a review of first results and prospects of the (AC^3) project. *Bull. Am. Meteorol. Soc.* **104**, E208 – E242 (2023).
7. Schneider, D. P. & Deser, C. Tropically driven and externally forced patterns of Antarctic sea ice change: reconciling observed and modeled trends. *Clim. Dyn.* **50**, 4599–4618 (2018).
8. Shu, Q. et al. Arctic Ocean amplification in a warming climate in CMIP6 models. *Sci. Adv.* **8**, eabn9755 (2022).
9. Previdi, M., Smith, K. L. & Polvani, L. M. Arctic amplification of climate change: a review of underlying mechanisms. *Environ. Res. Lett.* **16**, 093003 (2021).
10. Perovich, D. K. et al. Increasing solar heating of the Arctic Ocean and adjacent seas, 1979–2005: attribution and role in the ice-albedo feedback. *Geophys. Res. Lett.* https://doi.org/10.1029/2007GL031480 (2007).
11. Thackeray, C. W. & Hall, A. An emergent constraint on future Arctic sea-ice albedo feedback. *Nat. Clim. Chang.* **9**, 972–978 (2019).
12. Bintanja, R. & Selten, F. M. Future increases in Arctic precipitation linked to local evaporation and sea-ice retreat. *Nature* **509**, 479–482 (2014).
13. Feldl, N., Po-Chedley, S., Singh, H. K. A., Hay, S. & Kushner, P. J. Sea ice and atmospheric circulation shape the high-latitude lapse rate feedback. *npj Clim. Atmos. Sci.* **3**, 41 (2020).
14. Cohen, J. et al. Recent Arctic amplification and extreme mid-latitude weather. *Nat. Geosci.* **7**, 627–637 (2014).
15. Coumou, D., Petoukhov, V., Rahmstorf, S., Petri, S. & Schellnhuber, H. J. Quasi-resonant circulation regimes and hemispheric synchronization of extreme weather in boreal summer. *Proc. Natl. Acad. Sci. USA*. **111**, 12331–12336 (2014).
16. Hoskins, B. J., McIntyre, M. E. & Robertson, A. W. On the use and significance of isentropic potential vorticity maps. *Q. J. R. Meteorol. Soc.* **111**, 877–946 (1985).
17. Kornhuber, K. et al. Amplified Rossby waves enhance risk of concurrent heatwaves in major breadbasket regions. *Nat. Clim. Chang.* **10**, 48–53 (2020).
18. Cohen, J. et al. Divergent consensuses on Arctic amplification influence on midlatitude severe winter weather. *Nat. Clim. Chang.* **10**, 20–29 (2020).
19. Goosse, H. et al. Quantifying climate feedbacks in polar regions. *Nat. Commun.* **9**, 1919 (2018).
20. Ye, K. & Messori, G. Inter-model spread in the wintertime Arctic amplification in the CMIP6 models and the important role of internal climate variability. *Glob. Planet. Change* **204**, 103543 (2021).
21. Khosravi, N. et al. The Arctic Ocean in CMIP6 models: Biases and projected changes in temperature and salinity. *Earth's Future* **10**, e2021EF002282 (2022).
22. Taylor, P. C. et al. Process drivers, inter-model spread, and the path forward: A review of amplified arctic warming. *Front. Earth Sci.* **9**, 758361 (2022).
23. Kidston, J. et al. Stratospheric influence on tropospheric jet streams, storm tracks and surface weather. *Nat. Geosci.* **8**, 433–440 (2015).
24. Butler, A. H. et al. Defining sudden stratospheric warmings. *Bull. Am. Meteorol. Soc.* **96**, 1913–1928 (2015).
25. Domeisen, D. I. V. et al. The role of the stratosphere in subseasonal to seasonal prediction: 2. Predictability arising from stratosphere-troposphere coupling. *J. Geophys. Res. Atmos.* **125**, e2019JD030923 (2020).
26. Zhang, J., Orsolini, Y. J., Limpasuvan, V. & Ukita, J. Impact of the Pacific sector sea ice loss on the sudden stratospheric warming characteristics. *npj Clim. Atmos. Sci.* **5**, 74 (2022).
27. Roy, R. & Kuttippurath, J. The dynamical evolution of sudden stratospheric warmings of the Arctic winters in the past decade 2011–2021. *SN Appl. Sci.* **4**, 105 (2022).
28. Charney, J. G. & Drazin, P. G. Propagation of planetary-scale disturbances from the lower into the upper atmosphere. *J. Geophys. Res.* **66**, 83–109 (1961).
29. Andrews, D. G., Holton, J. R. & Leovy, C. B. Middle atmosphere dynamics, Vol. 40. In *International Geophysics Series* (Academic Press, 1987).
30. Kumar, A., Karami, K. & Jacobi, C. A 45-year climatological study of Arctic stratospheric polar vortex dynamics and morphology using ERA5 data (1979–2023). *Clim. Dyn.* **63**, 403 (2025).
31. Tomikawa, Y. et al. Growth of planetary waves and the formation of an elevated stratopause after a major stratospheric sudden warming in a T213L256 GCM. *J. Geophys. Res. Atmos.* **117**, D16101 (2012).
32. Lee, S. H., Butler, A. H. & Manney, G. L. Two major sudden stratospheric warmings during winter 2023/2024. *Weather* **80**, 45–53 (2025).
33. Ayarzagüena, B. et al. No robust evidence of future changes in major stratospheric sudden warmings: a multi-model assessment from CCMI. *Atmos. Chem. Phys.* **18**, 11277–11287 (2018).
34. Hersbach, H. et al. The ERA5 global reanalysis. *Q. J. R. Meteorol. Soc.* **146**, 1999–2049 (2020).
35. Vallis, G. K. *Atmospheric and Oceanic Fluid Dynamics*, 2nd edn. (Cambridge University Press, 2017).
36. Held, I. M. & Hoskins, B. J. Large-scale eddies and the general circulation of the troposphere. *Adv. Geophys.* **28**, 3–31 (1985).
37. Holton, J. R. An introduction to dynamic meteorology. In *International Geophysics Series*, Vol. 88, 4th edn (Elsevier Academic Press, 2004).
38. Juckes, M. N. Quasigeostrophic dynamics of the tropopause. *J. Atmos. Sci.* **51**, 2756–2768 (1994).
39. Simmonds, I. & Lim, E.-P. Biases in the calculation of Southern Hemisphere mean baroclinic eddy growth rate. *Geophys. Res. Lett.* **36**, L01703 (2009).
40. Zeitlin, V. *Geophysical Fluid Dynamics: Understanding (Almost) Everything with Rotating Shallow Water Models*, 1st edn (Oxford University Press, 2018).
41. Rostami, M., Bowen, Z. & Stefan, P. On the genesis and dynamics of Madden–Julian oscillation-like structure formed by equatorial adjustment of localized heating. *Q. J. R. Meteorol. Soc.* **148**, 3788–3813 (2022).
42. Rostami, M., Stefan, P., Fallah, B. & Fazel-Rastgar, F. Aeolus 2.0's thermal rotating shallow water model: a new paradigm for simulating extreme heatwaves, westerly jet intensification, and more. *Phys. Fluids* **37**, 016604 (2025).
43. Rostami, M. & Zeitlin, V. An improved moist-convective rotating shallow-water model and its application to instabilities of hurricane-like vortices. *Q. J. R. Meteorol. Soc.* **144**, 1450–1462 (2018).

Acknowledgements

This work was supported by the National Natural Science Foundation of China under grant 42230803. Additional support for J.G. was provided by the National Key Research and Development Program of China (grant no. 2025YFE0113400). M.H. gratefully acknowledges the Alexander von Humboldt Foundation for awarding the George Forster Experienced Researcher Fellowship and its support.

Author contributions

M.R. led the conceptualisation, developed the theoretical framework, performed the CMIP6 analysis and data analysis, and wrote the original draft. B.F. contributed to the conceptualisation, developed the methodology, performed the CMIP6 analysis, and contributed to writing the original draft and reviewing the manuscript. L.-Y.F. supervised the project and contributed to writing the original draft and reviewing the manuscript. F.F.-R. and M.H. contributed to the investigation and reviewed the manuscript. S.H. contributed to the investigation and reviewed the manuscript. J.G. contributed to the methodology, developed the analysis code and visualisation tools, and reviewed the manuscript.

Competing interests

The authors declare no competing interests.

Additional information

Supplementary information The online version contains supplementary material available at https://doi.org/10.1038/s41612-026-01439-z.

Correspondence and requests for materials should be addressed to Masoud Rostami or Li-Yun Fu.